Monthly Notices
of the
ROYAL ASTRONOMICAL SOCIETY

MNRAS **505,** 1509–1529 (2021)
Advance Access publication 2021 May 6

https://doi.org/10.1093/mnras/stab1226

The nature of sub-millimetre galaxies I: a comparison of AGN and star-forming galaxy SED fits

T. Shanks [1]★ B. Ansarinejad [1] R. M. Bielby [1] I. Heywood [2] N. Metcalfe[1] and L. Wang[3]

[1]*CEA, Physics Department, Durham University, South Road, Durham DH1 3LE, UK*
[2]*Astrophysics, Department of Physics, University of Oxford, Keble Road, Oxford OX1 3RH, UK*
[3]*SRON Netherlands Institute for Space Research, Landleven 12, NL-9747 AD, Groningen, the Netherlands*

Accepted 2021 April 25. Received 2021 April 25; in original form 2020 October 14

ABSTRACT

High-redshift sub-millimetre galaxies (SMGs) are usually assumed to be powered by star formation. However, it has been clear for some time that >20 per cent of such sourcesbrighter than ≈3 mJy host quasars. Here, we analyse a complete sample of 12 sub-mm LABOCA/ALMA 870-μm sources in the centre of the William Herschel Deep Field (WHDF) with multiwavelength data available from the X-ray to the radio bands. Previously, two sources were identified as X-ray-absorbed quasars at $z = 1.32$ and $z = 2.12$. By comparing their spectral energy distributions (SEDs) with unabsorbed quasars in the same field, we confirm that they are dust reddened although at a level significantly lower than implied by their X-ray absorption. Then, we compare the SEDs of all the sources to dust-reddened AGN and star-forming galaxy models. This optical/NIR comparison combined with Spitzer MIR colours and faint *Chandra* X-ray detections shows that 7/12 SMGs are best fitted with an obscured quasar model, a further 3/12 show no preference between AGN and star-forming templates, leaving only a $z = 0.046$ spiral galaxy and one unidentified source. So in our complete sample, the majority (10/12) of bright SMGs are at least as likely to fit an AGN as a star-forming galaxy template, although no claim is made to rule out the latter as SMG power sources. We then suggest modifications to a previous SMG number count model and conclude that obscured AGN in SMGs may still provide the dominant contribution to both the hard X-ray and sub-millimetre backgrounds.

Key words: quasars – sub-millimetre: galaxies – submillimetre: diffuse background; X-rays: diffuse background.

1 INTRODUCTION

It is now more than two decades since the first blank field surveys using the Submillimetre Common-User Bolometer Array on the James Clerk Maxwell Telescope revealed the existence of large numbers of highly luminous far-infrared (FIR) sources, usually referred to as sub-millimetre galaxies or SMGs (Smail, Ivison & Blain 1997; Barger et al. 1998). These objects were quickly found to be at high redshift and to be heavily obscured by dust (e.g. Blain et al. 2002). But the identity of luminous sub-millimetre sources is still controversial. The standard view is that they are hyper-luminous starburst galaxies, seen in an obscured phase of their evolution (e.g. Alexander et al. 2005). In this interpretation, they may be involved in the origin of early-type galaxies. But because of their high star formation rate (SFR) and mass, they then present a problem for the standard cosmology that still has to invoke a 'top-heavy' stellar initial mass function (IMF) in starbursts to explain them (Baugh et al. 2005; Lacey et al. 2008). Bars and even spiral arms have been detected in ALMA (Atacama Large Millimeter/submillimeter Array) images and claimed as support for the star-forming galaxy (SFG) picture (Hodge et al. 2016; Gullberg et al. 2019). However, these features are always seen only on scales an order of magnitude smaller than seen in local classical spiral galaxies.

An alternative hypothesis is that the bright sub-millimetre population is mainly powered by active galactic nuclei (AGN). Many sub-millimetre sources contain AGN but the usual view is that they are sub-dominant to star formation in powering these sources (e.g. Laird et al. 2010). But there are strong arguments for considering obscured AGN as being candidates for powering the SMG population. Obscured quasars are the primary candidates to explain the 'missing' hard X-ray background (e.g. Comastri et al. 1995). Since these highly absorbed sources are likely to be dust-rich objects, they would be expected to have substantial luminosities in the infrared where the reprocessed light is emitted. Obscured AGN models have been previously shown to give a reasonable fit to the bright end of the sub-millimetre source counts, while SFGs are expected to make the dominant contribution at fainter fluxes (see fig. 12 of Hill & Shanks 2011a following Gunn & Shanks 1999). If the sub-millimetre emission results from a dust torus irradiated by an AGN instead of star formation, it must lie far enough (≈0.5 kpc) from the central engine to maintain a cool (∼35 K) temperature and simple torus models confirm feasibility (e.g. Andreani, Franceschini & Granato 1999; Kuraszkiewicz et al. 2003; Siebenmorgen, Voshchinnikov & Bagnulo 2014). Hill & Shanks (2011a) and Hill & Shanks (2011b) also showed that an obscured AGN model also fitted the bimodality of the Herschel Spectral and Photometric Imaging Receiver (SPIRE) $n(z)$, with the star-forming and AGN components dominating at low and high z, respectively, while predicting that ≈20 per cent of bright SMGs should be X-ray sources even at soft energies.

★ E-mail: tom.shanks@durham.ac.uk

There now exists clear evidence of AGN activity in 20–40 per cent of bright sub-millimetre sources, confirming this prediction. First, early 1.″4 ALMA imaging by Wang et al. (2013) found that 17 ± 6 per cent of Extended Chandra Deep Field South (ECDFS) SMGs are X-ray sources. More recently, Cowie et al. (2018) in their Super GOODs ALMA survey found evidence for bright SMGs being dominated by hard X-ray sources while fainter sub-mJy SMGs were dominated by soft X-ray sources more consistent with SFGs. Franco et al. (2018) found that at least 40 per cent of bright SMGs host an X-ray AGN, compared to ≈14 per cent for other galaxies of similar mass and redshift. Finally, Stach et al. (2019) find that 18 ± 10 per cent of bright SMGs are AGN as identified by power-law SEDs and other diagnostics. These significant AGN fractions are all the more remarkable, given the 2−3× more near-Compton-thick AGN that may be wholly invisible even to ≈10-keV X-ray surveys. We also note that AGN-powered SMG number count models generally assume that fainter sub-mJy SMGs will be dominated by SFGs while the >1 mJy luminous SMG population will be dominated by AGN-powered sources, consistent with these recently reported results. With the advent of high-resolution ALMA observations, sub-millimetre source counterparts can be more accurately identified and then tested for the presence of an active nucleus. In about ≈20 per cent of cases, broad or high-excitation emission lines can be seen. In the other ≈80 per cent, we can now check how well a dust-obscured AGN spectral energy distribution (SED) fits the ALMA counterpart in the optical/IR.

Here, we shall test how well a sample of 12 SMGs, complete to ≈3 mJy at 870 μm, can be fitted with dust-obscured AGN template SEDs. They were originally identified in an 11.′4 diameter area of the William Herschel Deep Field (WHDF, Metcalfe et al. 1996, 2001, 2006) by Bielby et al. (2012) using the Large APEX Bolometer Camera (LABOCA) on the Atacama Pathfinder Experiment (APEX) telescope. We shall compare the quality of these fits to those for similarly absorbed SFGs. We are helped by having new, high-resolution, high signal-noise (S/N) ALMA imaging for eight of the 12 sources to help identify counterparts. These eight ALMA sources in themselves form a complete sample within the original 7′ × 7′ of the original WHDF (see figs 2 and 3 of Heywood et al. 2013), although there are no ALMA data for the nearby spiral galaxy LAB-06. All 12 sources are contained in the extended 16′ × 16′ WHDF area where there is a large amount of multiwavelength data. We shall fit optical and near-infrared/mid-infrared (NIR/MIR) data to estimate redshift and dust absorption and FIR and sub-millimetre data to estimate dust temperatures and masses. Although we shall not model or fit the WHDF *Chandra* X-ray data, these will also be vital for identifying several of our sources.

Therefore in Section 2, we describe the multiwavelength data now available in the WHDF. In Section 3, we detail our SED-fitting procedures before reporting the results of fitting AGN and star-forming templates to the 12 individual SMG SEDs in Section 4. In Section 5, we discuss how well the AGN and star-forming template fits compare overall and the implications for the nature of sub-millimetre sources. Finally, in Section 6, we present our conclusions.

We note that the analysis of the size, structure, and SFR surface brightness of the seven sources observed by ALMA will be presented in Paper II (see Ansarinejad 2020 for preliminary results). There, the analysis of the ALMA observations of four $z > 6$ QSOs (Quasi-Stellar Objects or quasars) (Carnall et al. 2015; Chehade et al. 2018) will also be presented to complement the interpretation of the WHDF SMGs. Finally, Paper III will discuss the FIR properties from the Herschel HerMES Large Mode Survey (HeLMS) of the full population of 16 X-ray QSOs found by *Chandra* in the WHDF (Vallbe Mumbru 2004; Bielby et al. 2012) plus the four $z > 6$ quasars detected by ALMA.

2 DATA

The WHDF is a 7′ × 7′ sky area (extended to 16′ × 16′) at RA (J2000) = 00h22m33.3s, Dec = +00d20m57s, initially observed in the optical at the William Herschel 4.2-m telescope (Metcalfe et al. 2001) and in the NIR at the Calar Alto 3.5-m telescope (Metcalfe et al. 2006) to provide UBRIZHK photometry to $B \approx 28$. Subsequently, it was observed with deep *Chandra* X-ray data, *Hubble Space Telescope* (*HST*) *i*-band imaging (Böhm & Ziegler 2007; Fritz, Böhm & Ziegler 2009), Spitzer IRAC Equatorial Survey (SPIES) 3.6- and 4.5-μm imaging (Timlin et al. 2016), and in the Herschel HeLMS survey at 250, 350, and 450 μm (e.g. Wang et al. 2015). It has also been observed with deep LABOCA + ALMA exposures at sub-millimetre wavelengths (Bielby et al. 2012) and at 8.4 GHz (3.57 cm) with the Karl G. Jansky very large array (VLA) (Heywood et al. 2013). A summary of the fluxes in each band for the SMGs can be found in Table 1. Further details including the flux errors, the coordinates of source counterparts, and their magnitudes and colours are given in Tables A2–A4 in Appendix A.

Although WHDF was one of the earliest deep fields to be observed with CCD detectors, clearly there are now other fields with wider and deeper coverage in more high-resolution bandpasses from *HST*, such as the GOODS fields (Dickinson, Giavalisco & GOODS Team 2003) and successors, e.g. CDFS (Luo et al. 2017), the *HST* UDF (Beckwith et al. 2006), the COSMOS field (Le Fèvre et al. 2015), CANDELS (Grogin et al. 2011), etc. Nevertheless, for our current purpose, the availability of high-resolution 0.″09, high S/N FIR data from ALMA in the WHDF is ideal for checking for counterparts and looking for low surface brightness features such as bars and spiral arms. Such data are still only rarely available in the other deep fields. The availability of 75-ksec *Chandra* X-ray data is also vital for diagnosing AGN. Again, other fields such as CDFS have 7-Ms exposures available and their deepest exposure per pixel is effectively ≈50× that in WHDF. Nevertheless, in searching for AGN X-ray signatures from typical bright SMGs, we shall see that our *Chandra* combination of exposure time, resolution, and low background is ideal. Fainter exposures are dominated by X-ray galaxies below the usual $>10^{42}$ ergs s^{-1} AGN limit. So, with WHDF, we can develop the analysis methods to see if a hypothesis of significant AGN contribution to SMGs passes this first test that may motivate similar analyses of data sets such as ALESS (Karim et al. 2013; Hodge et al. 2013) in ECDFS (Weiß et al. 2009) with similar ALMA coverage but deeper *HST* and *Chandra* data or AS2UDS (Dudzevičiūtė et al. 2020) with many more ALMA sources albeit observed at lower resolution, together with deeper ground-based *K*-band data.

2.1 FIR and sub-millimetre data

The original 870-μm survey in the WHDF was made in 2008 August and 2009 May using the LABOCA instrument on the APEX telescope at the Chajnantor site in Chile. The observations were fully described by Bielby et al. (2012), who compared 11 detected sub-millimetre sources in a central 16′ diameter area of the WHDF to the *Chandra* X-ray sources, mainly identified as quasars (Vallbe Mumbru 2004). The sub-millimetre sources were detected as a complete sample down to 3.3 mJy/beam. Only three sub-millimetre sources were optically identified, LAB-05 and LAB-11 as X-ray-absorbed quasars at $z = 1.32$ and $z = 2.12$ and LAB-06 as a spiral galaxy at $z = 0.046$.

Table 1. ALMA/LABOCA counterpart source fluxes and upper limits in mJy. See Tables A4, A2, and A3 for coordinates of counterparts (and companions) to the sub-millimetre sources. Flux errors are available in the Supplemental Data. Rows 1–3 give the *Chandra* X-ray 0.5–1.2, 1.2–2.0, and 2.0–7.0 keV fluxes, rows 4–9 the WHDF UBRIZHK data, and rows 9, 12, 13, and 14 list the W1, W2, W3, W4 band fluxes from WISE. Rows 10 and 11 give the 3.6- and 3.5-μm fluxes from SPIES and rows 15–16 list the HeLMS FIR fluxes. Row 17 gives the LABOCA sub-millimetre fluxes in mJy/beam except for LAB-12 where the ALMA flux is given. Row 17 gives the VLA 8.4-GHz flux.

$\lambda(\mu m)$	LAB-1	LAB-2	LAB-3	LAB-4	LAB-5	LAB-6	LAB-7	LAB-8	LAB-9	LAB-10	LAB-11	LAB-12
3.26e-4	6.13e-8	<1.9e-8	3.50e-9	<1.9e-8	1.73e-7	<1.9e-8	<1.9e-8	<1.9e-8	<1.9e-8	<1.9e-8	3.98e-7	<1.9e-8
7.95e-4	3.02e-8	<3.6e-8	9.14e-8	2.89e-8	3.71e-7	<3.6e-8	<3.6e-8	<3.6e-8	<3.6e-8	<3.6e-8	1.04e-7	<3.6e-8
1.14e-3	<3.2e-8	<3.2e-8	<3.2e-8	6.40e-8	6.51e-8	<3.2e-8	<3.2e-8	<3.2e-8	<3.2e-8	<3.2e-8	<3.2e-8	<3.2e-8
0.375	<3.4e-5	<3.4e-5	8.63e-5	<3.4e-5	4.13e-4	0.15	2.91e-4	2.00e-4	<2.5e-4	<3.4e-3	1.21e-3	<3.4e-5
0.45	5.45e-5	4.45e-5	2.83e-4	<2.7e-5	7.59e-4	0.39	6.43e-4	2.42e-4	<1.7e-4	2.23e-4	1.53e-3	<2.7e-5
0.65	2.01e-4	1.50e-4	6.55e-4	<5.8e-5	1.13e-3	1.15	3.16e-3	1.66e-4	1.7e-4	7.73e-4	2.94e-3	<9.1e-5
0.80	0.72e-4	1.79e-4	6.61e-4	<7.6e-5	1.60e-3	1.50	4.70e-3	5.25e-4	<5.25e-4	–	6.08e-3	1.77e-4
0.90	–	–	–	–	–	1.94	4.06e-3	–	–	–	7.52e-3	–
1.65	2.21e-3	<7.7e-4	1.89e-3	1.92e-3	1.06e-2	3.37	9.55e-3	<1.9e-3	3.84e-3	<7.7e-2	3.02e-2	3.87e-3
2.20	–	–	–	–	1.29e-2	2.83	–	–	–	–	4.21e-2	7.45e-3
3.37	–	–	–	–	–	1.00	–	–	–	–	8.60e-2	–
3.55	2.00e-2	<2.0e-3	2.93e-3	9.15e-3	3.88e-2	1.72	9.36e-3	<2.0e-3	8.21e-3	1.14e-2	0.11	2.36e-2
4.49	1.42e-2	<2.0e-3	<2.0e-3	2.04e-2	4.87e-2	1.23	6.56e-3	3.16e-3	9.01e-3	1.82e-2	0.16	2.15e-2
4.62	–	–	–	–	–	0.67	–	–	–	–	0.20	–
12.01	–	–	–	–	–	3.70	–	–	–	–	0.75	–
22.19	–	–	–	–	–	4.77	–	–	–	–	4.04	–
250	40.67	20.60	<20	<20	32.52	129.77	91.10	42.49	<20	22.18	44.0	<20
350	32.07	<20	<20	<20	46.14	39.59	72.04	54.0	<20	27.74	<20	<20
500	37.72	24.23	<20	<20	42.34	25.57	61.61	39.64	<20	<20	<20	<20
850	5.1	4.3	5.4	4.1	4.0	3.9	8.2	6.2	5.1	3.3	3.4	1.68
35461	–	1.46e-2	–	–	3.75e-2	2.01e-1	–	–	–	–	4.6e-2	–

A complete, flux-limited (but excluding LAB-06) subset of the LABOCA sources, LAB-01, -02, -03, -04, -05, -10, and -11, in the central $7' \times 7'$ of the WHDF was then targeted by ALMA on 2016 October 11, with the 12-m Array in a configuration, which yielded 870-μm continuum images at $0.''095$ resolution and a maximum recovered scale of $0.''926$. The exposure times were 1572 s each, long enough to detect any diffuse emission including spiral arms and bars surrounding the sub-millimetre core (see Paper II). These observations reached an 870-μm surface brightness rms of 65 μJy/beam over an $\approx 17''$ field of view. All seven targets were strongly detected, with LAB-11 revealing a second sub-millimetre source (named LAB-12) at $\approx 5''$ from the main LAB-11 source. The ALMA data were reduced using CASA imaging pipeline and then fitted for ellipticity, flux, and position using the IMFIT package. Full details will be given in Paper II.

The Herschel HeLMS survey (Oliver et al. 2012; Asboth et al. 2016) covers the WHDF within its full 302 deg^2 area. HeLMS was observed in two fast-mode scans by Herschel SPIRE in the 250-, 350-, and 500-μm bands, reaching almost the confusion limits. The resolution was $18''$, $25''$, and $36''$ full width at half-maximum (FWHM) with $6''$, $8.''33$, and $12''$ pixels, resampled to $6''$ in the final maps. The nominal 1σ noise (instrument + confusion) limits are 15.61, 12.88, and 10.45 mJy in the 250-, 350-, and 450-μm bands. Here, we assume detection limits of >20 mJy in each band. The 12 LABOCA sources were cross-correlated with these Herschel catalogues and FIR sources were taken as counterparts within radii of $20''$, $30''$, and $40''$ at 250, 350, and 500 μm. The resulting source fluxes are listed in Table 1 and their coordinates in Table A4.

2.2 *Chandra* X-ray data

The *Chandra* X-ray data on the WHDF turn out to be crucial in establishing the identity of several of our sub-millimetre sources. *Chandra* observed the WHDF with the ACIS-I detectors for 75 ksec (71 ksec on-sky). These data and their reduction and analysis were presented by Vallbe Mumbru (2004) and an initial comparison to the WHDF LABOCA sources was carried out by Bielby et al. (2012). The X-ray observations were made in December 2000 with Chandra's ACIS-I detector. The observation reaches fluxes of 4×10^{-16} erg cm^{-2} s^{-1} in the soft 0.5–2 keV band, 3×10^{-15} erg cm^{-2} s^{-1} in the hard 2–8 keV band, and 1×10^{-15} erg cm^{-2} s^{-1} in the total 0.5–8 keV band, and resolves >70 per cent of the hard X-ray background. The ACIS-I pointing centre was 00 h22 m33.3 s, +00d20m55.0s (J2000), and the *Chandra* observation id was 900079. Vallbe Mumbru (2004) detected 150 sources with $S/N > 2$ in the total band. As reported by Bielby et al. (2012), only two sources were identified with X-rays to this limit to $S/N > 3$, LAB-05, (whdfch008), and LAB-11, (whdfch007). These X-ray sources have optical spectroscopy that identifies them as $z = 1.32$ and $z = 2.12$ X-ray-absorbed QSOs.

Here, we re-analyse these X-ray data looking at the ALMA source positions for X-ray photons to a formal $S/N > 1.43$ (i.e. 90 per cent confidence) that the source flux is non-zero in one of three bands, 0.5–1.2, 1.2–2.0, and 2–7 keV, using 'ciao' routine *srcflux*. At these limits, we detected LAB-01, LAB-03, and LAB-04 in at least one of these bands, as well as LAB-05 and LAB-11. We also detected X-rays at optical positions within the LABOCA $\approx 11''$ radius error circles for a further two sources: LAB-06 and LAB-07. In the latter case, there are two possible optical counterparts with X-rays, named LAB-07-1 and LAB-07-3.

We then tested for the significance of these detections by making *srcflux* measurements in a randomly chosen 10×10 grid at $\approx 40''$ intervals in the central $7' \times 7'$ ACIS-I area. No detections were made in any band where the formal 90 per cent confidence interval included zero. The faintest 'sources' detected randomly had 1.13×10^{-5} c/s (i.e. $\approx$1 count in 71 ksec) or 8.5×10^{-17} erg cm^{-2} s^{-1} in the 0.5–1.2 keV band, 1.07×10^{-5} c/s or 5.83×10^{-17} erg cm^{-2} s^{-1} in the 1.2–2 keV band, and 1.72×10^{-5} c/s or 1.07×10^{-15} erg cm^{-2} s^{-1} in the 2–7 keV band.

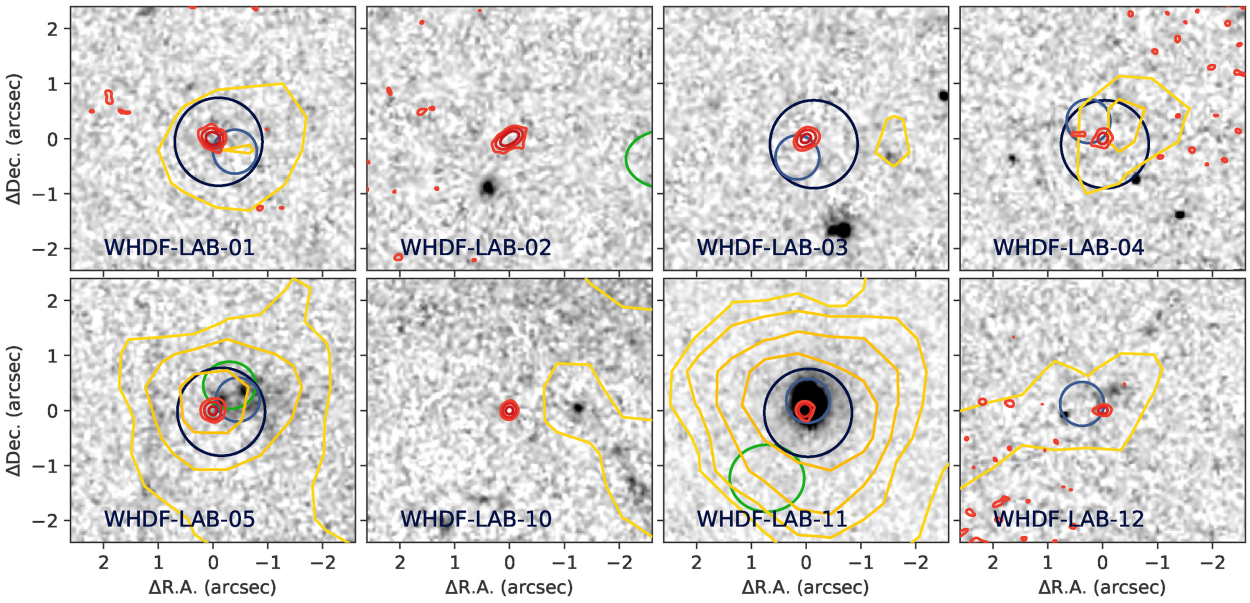

Figure 1. Finding charts (North: top, East: left) centred on eight ALMA sources obtained by combining the *HST i* + ALMA + SPIES (3.6 μm) data. The *HST i* image is shown in grey-scale, ALMA in red contours, and SPIES in yellow/orange contours. Also marked are detected sources in WHDF *H* band (pale blue), *Chandra* X-ray (dark blue), and VLA 8.4 GHz (green).

We note that these latter flux limits indicate that they are 99 per cent flux limits when the *srcflux* computed flux limit was at the 90 per cent level. We suggest that this is due to the background level in these early *Chandra* observations being low at the level of 0.05 counts per pixel in the two softer bands and 0.15 counts/pixel in our hard band. With ACIS-I having 0.″492 pixels and 50 per cent of light encircled within a 0.″75 radius within the 7′ WHDF field ACIS-I, there are only ≈7 pixels per resolution element giving a background count of ≈0.35 counts in the softer bands and ≈1 count in the hard band. This means that a single count is usually enough to establish a detection in the two softer bands and 1–2 counts in the hard band. So in LAB-01, we detect one count at 0.5–2keV and two counts at 2–7keV, in LAB-03, we detect two counts at 1.2–2keV, and in LAB-04, we detect one count at 0.5–1.2 keV and one count at 1.2–2keV. Clearly, although the error on each flux will be of order of 100 per cent of the signal, the significance of detection in each case is secure. This is confirmed empirically by our random flux measurements on the real *Chandra* data. The X-ray fluxes are listed in Table 1 and exact coordinates in Tables A2 and A3.

2.3 Optical/NIR data

To identify optical sources detected in WHDF *ubriz* images with seeing in the range of 1.″0−1.″5 down to $S/N = 3$, we take $\Delta\theta = 2.5 \times 0.6\theta(S/N)^{-1}$ (Bielby et al. 2012) where seeing $\theta = 1.''5$ gives $\Delta\theta = 0.''75$. Noting that all ground-based WHDF images have 0.″4 pixels, we have corrected systematics in the original WHDF astrometry by comparing WHDF *r* catalogue astrometry against overlapping DECam Legacy Survey (DECaLS) astrometry. We found that $RA_{DECaLS} = RA_{WHDF} + 0.''49 \pm 0.''012$, $Dec_{DECaLS} = Dec_{WHDF} - 0.''35 \pm 0.''012$. The original WHDF *H* catalogue shows slightly different offsets relative to DECaLS: $RA_{DECaLS} = RA_H + 0.''15 \pm 0.''0.012$, $Dec_{DECaLS} = Dec_H - 0.''37 \pm 0.''012$. The *HST i* image offsets to DECaLS are smaller and can be neglected. Because of the remaining uncertainties on *r* and *H* WHDF coordinate offsets, we shall generally have to be flexible in interpreting offsets to ALMA, VLA, and *HST* positions. Note that in Tables A2 and A3 and Figs 1 and 2 and throughout, we shall now always use the WHDF *r* and *H* coordinates corrected to the DECaLS astrometric frame.

Given these astrometric issues, here for the eight ALMA sources, we follow Bielby et al. (2012) and take $\Delta\theta < 1.''3$ or ≈3 pixels as the upper limit on WHDF–ALMA separations. Since the galaxy sky density at the WHDF 3σ limit of $r = 26.3$ is $\approx 3 \times 10^5 \mathrm{deg}^{-2}$, this means that in a circle of radius 1.″3 around an ALMA source, the expected number of optical sources is ≈0.12. So, we expect only contamination by ≈1 faint WHDF source in our eight ALMA source counterparts. The WHDF coordinate corrections are less important for the sources with only, less accurate, LABOCA positions i.e. LAB-06, −07, −08, and −09. For these, we take the error circle radii, $\Delta\theta$, listed individually in table 1 of Bielby et al. (2012). The resulting fluxes for the WHDF counterparts in *ubriz* (where available) are given in Table 1.

The WHDF *H*-band data in the central 7′ × 7′ from a 14.25-h Calar Alto OmegaPrime exposure have 0.″9 seeing with 0.″396 pixels and are particularly deep, reaching $H_{Vega} = 22.9$ at 3σ (Metcalfe et al. 2006). The central WHDF *K*-band data are less deep, reaching only $K'_{Vega} = 20.7$ in similar seeing in a 0.9-h exposure with the same instrument (Metcalfe et al. 2006). For the *HST* Advanced Camera for Surveys 2450-s exposure *i*-band frame on WHDF (Böhm & Ziegler 2007), the resolution is 0.″1 and the pixel size is 0.″05, but we still allow a radius of $\Delta\theta = 0.''65$ to allow for astrometry systematics. Again, the WHDF *HK* and *HST i*-band fluxes are listed in Table 1.

2.4 SPIES MIR data

Spitzer 3.6- and 4.5-μm data from the Spitzer IRAC Equatorial Survey (SPIES, Timlin et al. 2016) cover ≈115 deg^2 of SDSS Stripe 82 and therefore contain the whole WHDF within this equatorial region. The SPIES data reach 5σ depths of 6.13 μJy and 5.75 μJy at 3.6 μm and 4.5 μm, respectively. Here, for our fits, we set ≈2σ flux limits of 2 μJy in each band. The SPIES pixel size of 0.″6 is half of the Spitzer IRAC pixel size due to image dithering. The Pont Spread

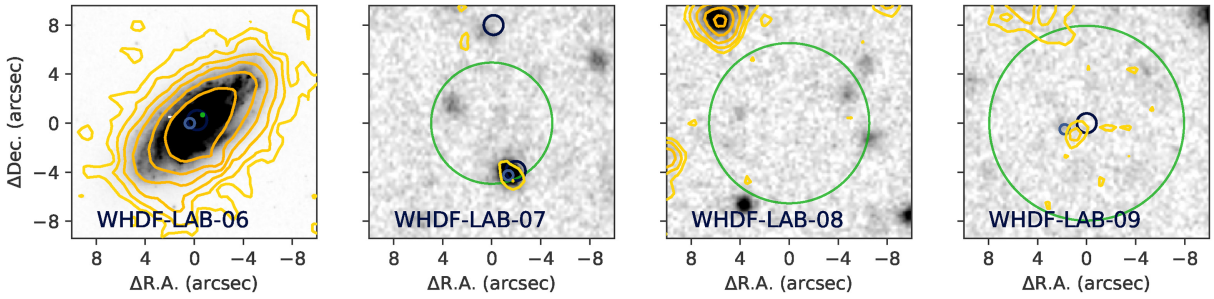

Figure 2. Finding charts (North: top, East: left) for LABOCA-only sources centred on the LABOCA position in the *HST* *i*-band image for LAB-06 and the WHDF *r*-band image for the three others. The LABOCA error circles are shown in green. SPIES (3.6 μm) data are shown by the yellow contours. X-ray detections are shown as black circles. *H*-band detections are shown as blue ellipses. Our preferred candidate counterpart for LAB-07 (LAB-07-3) is the most Southerly object in the LABOCA error circle.

Function (PSF) FWHM corresponds to the 'warm' IRAC values of 1.″95 in the 3.6-μm detector and 2.″02 in the 4.5-μm detector. All three catalogues including the Dual detection, 3.6-μm only and 4.5-μm only, were used. 2839 matches to SPIES data were found to the 14 527 $r < 25.9$ objects in the $16' \times 16'$ extended WHDF area. No deep, longer wavelength data at 8, 12, 65, 100 μm are available and this will clearly make it difficult to detect hotter temperature dust components in our SMG SEDs. The only data at longer MIR wavelengths in the WHDF are given by the much shallower WISE data in the W3 and W4 bands at 12 and 22 μm (Wright et al. 2010). Only LAB-11 is detected in these bands. See Table 1 for the SMG counterpart fluxes at 3.6 and 4.5 μm.

2.5 VLA radio data

VLA data for the central $7' \times 7'$ at 8.4 GHz (3.57cm) were reported by Heywood et al. (2013). These radio data were aimed at helping to identify the LABOCA source counterparts and were made in the most compact D-configuration in 2010 March–June, with a 30-h exposure time. Over most of the central $7' \times 7'$ WHDF field, the observations achieved a spatial resolution of 8″ FWHM and an rms background noise of 2.5 μJy. 41 sources were detected at $>4\sigma$ of which 17 had primary beam-corrected flux densities. LAB-02, −05, −06, and −11 were identified as radio sources with LAB-05 and LAB-11 identity confirmed as X-ray-absorbed QSOs, LAB-06 as a low-redshift spiral galaxy, and LAB-02 remained optically unidentified. The VLA fluxes are again listed as the final entries in Table 1.

2.6 Source photometry

Finding charts giving the relative positions of these multiwavelength data are given for the ALMA sources in Fig. 1 and for the LABOCA-only sources in Fig. 2. The resulting multiwaveband source photometry is summarized in Table 1 from the X-ray to the radio. Wavelengths are given in microns and fluxes are given in mJy. Flux upper limits are given where there was no detection in a given band. Flux errors are given in Table A1. The details of how the counterparts were decided upon are included in the object-by-object description of the SED fits in Section 4.4. Coordinates and other details for source counterparts and companions are given in Tables A2–A4.

Again we note that the optical/NIR WHDF data on which Figs 1 and 2 are based have fewer *HST* bands than, e.g. the CDFS CANDELS field where the *HST* depth is also ≈1 mag deeper. However, we are fortunate to have the *HST* F814W band available to explore the morphology of any counterpart in the optical/UV. The CDFS field also has the advantage in having *HST* WFC3 *H*-band data at nominally 0.″15 resolution (although with 0.″13 pixel size) whereas the best *H*-band resolution is 0.″9 in the WHDF. But again, it turns out that only 1 out of 12 sub-mm sources are undetected in at least one of our bands. The WHDF ground-based depth is also highest in the *U*, *B* bands and this makes it vital to explicitly use flux upper limits in these bands when SED fitting. Clearly, we shall return to exploit the advantages of ALESS and AS2UDS data to test AGN fits if the WHDF results make this appear worthwhile.

We shall be referring to the 3.6- and 4.5-μm SPIES data throughout the following. We therefore first show a comparison between the distribution of 3.6-μm magnitudes (Vega-auto system) for the sub-millimetre sources and the 16 X-ray quasars listed by Bielby et al. (2012) in Fig. 3(a) and similarly for the 4.5-μm magnitudes in Fig. 3(b). Note that LAB-05 and LAB-11 that were previously identified as quasars are here counted in the quasars rather than SMGs. LAB-06 is also excluded from either population on the grounds of its low redshift and hence luminosity. We see that the broad-lined quasars are ≈10× brighter than the SMGs and we shall discuss the implications of this result in Section 5. Fig. 4 compares the [3.6]−[4.5] (Vega aperture 1) magnitude colours of the quasars and sub-millimetre sources. Here, we initially see that all but one of our sub-millimetre sources show similar colours to the quasars with [3.6]−[4.5] > 0.4, the limit used to select AGN by Stern et al. (2012). Again, these colours will be discussed as we assess the SED-fitting results in Section 4.4.

3 SED-FITTING METHOD

The method we use for SED fitting is maximum likelihood, *L*. Here, we broadly follow the method set out by Sawicki (2012), which deals with upper limits as well as detected fluxes, coded in Fortran. We note that we are minimizing $ln(L) \approx \chi^2/2$ so 1σ errors on derived parameters are approximately given where $ln(L) = ln(L_{min}) + 0.5 \times \Delta\chi^2(\nu)$ where $\Delta\chi^2 = 3.53, 4.72, 5.89$ for $\nu = 3$, 4, and 5 fitted parameters. When all fluxes are detected, this reduces to the usual χ^2 fit. Note that when there are upper limits involved, $ln(L)$ can numerically lie below zero, unlike for χ^2. We fit the SED-scaling parameter, *S*, in the optical-IR regime separately from the FIR-sub-millimetre range but add the likelihoods to get the best overall fit, analogous to adding χ^2 when all observed fluxes are detected. We do not SED-fit the X-ray data, which we regard as being beyond the scope of this study. However, X-ray detections remain a valuable diagnostic for distinguishing AGN and star-forming sources.

We first fit in the optical-NIR for absorption, A_V, and redshift, *z*, then we fit separately for a grey-body temperature plus redshift. More details are given in Paper II, but we essentially use equation (1)

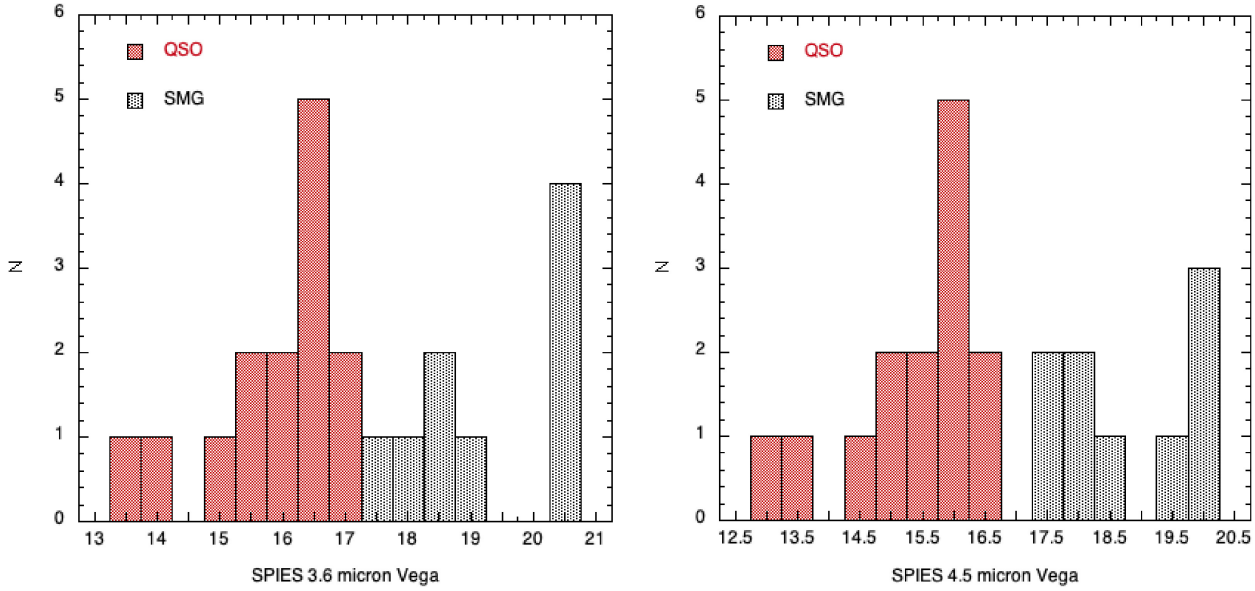

Figure 3. (a) Comparison between 3.6-μm apparent magnitudes of WHDF QSOs and SMGs, excluding LAB-06. The undetected LAB-02, -03, -08, and -10 SMGs are represented by upper limits in the 20.5 mag bin. (b) Comparison between apparent 4.5-μm apparent magnitudes of WHDF quasars and SMGs. The undetected LAB-02, -03, and -10 SMGs are represented by upper limits in the 19.75 mag bin.

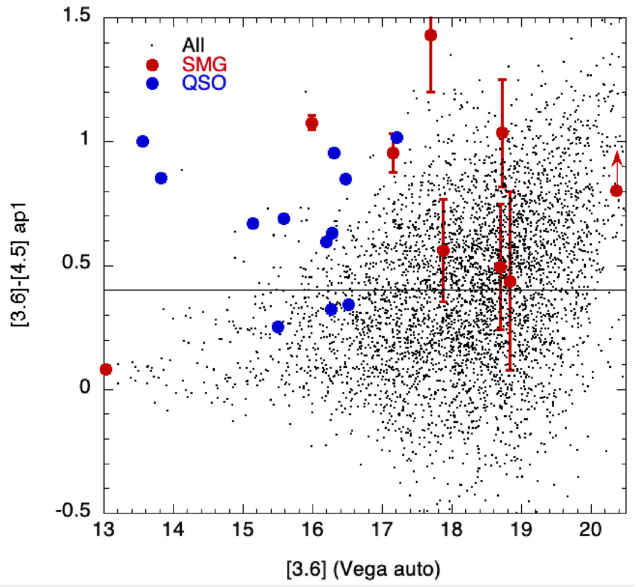

Figure 4. 3.6−4.5 μm: 3.6-μm colour-magnitude plot for all objects in WHDF area from SPIES data. Red dots mark WHDF SMGs with SPIES detections (i.e. excluding LAB-2, -3, and -10). LAB-08 with only a 4.5-μm detection is shown as an upper limit in 3.6 μm and a lower limit in [3.6]–[4.5] μm colour. Blue dots mark WHDF QSOs with *Chandra* X-ray detections. The horizontal line represents the $W1-W2 > 0.4$ limit recommended by Stern et al. (2012) for QSO selection and we note that all our SMGs with the exception of LAB-06 lie above this line.

of Dunne et al. (2000) with dust mass opacity coefficient, $\kappa = 0.077 \times (\nu/352.0e9)^{\beta}$ m^2 kg^{-1}, with emissivity index, $\beta = 1.8$, to estimate the dust mass, $M_{\rm d}$, given a dust temperature, T. For the $M_{\rm d}$ estimates, we assumed a cosmology with $\Omega_{\lambda} = 0.7$, $\Omega_{\rm m} = 0.3$, and $H_0 = 100$ km s^{-1} Mpc^{-1}. Then, we combine the two fits to derive an overall best-fitting redshift, dust temperature, and mass. This procedure usually leaves the best-fitting absorption, $A_{\rm V}$, unaffected.

We convert all data into mJy and then into νf_{ν} for fitting. We calculate $z = 0$ model values with wavelength and compare to observed values for the source with each spectral band's rest wavelength calculated for the tested redshift. The redshift range tested was $0 < z < 4.5$ at 0.1 redshift intervals. Other ranges were $0 < A_{\rm V} < 2.5$ mag at 0.25 mag intervals and $10 < T < 50$ K at 1 K intervals.

Since we are fitting five parameters, z, $A_{\rm V}$, T, and scaling factors $S_{\rm Opt/IR}$ and $S_{\rm FIR}$, we apply $\Delta\chi^2 > 5.89$ to give our 1σ errors following Press et al. (1992). This corresponds to $\Delta - ln(L) > 2.95$, which is required since we use the Maximum Likelihood estimates to derive parameter errors as well as the parameters themselves. For goodness-of-fit measures, we calculate χ^2 for the maximum likelihood model parameters. Here, we replace data upper limits by the upper limits themselves with errors also equal to the upper limit values, thus effectively treating all upper limits as 1σ detections.

4 SED-FITTING RESULTS

In making a comparison between AGN and SFG SMG fits, we first acknowledge that Dudzevičiūtė et al. (2020) have shown that, with enough assumed model components, it is certainly possible to get good χ^2 fits to their ≈700 SMGs with their SFG templates. da Cunha et al. (2015) list their model template parameters as including stellar populations' age, SFR, and metallicity plus stochastic SF bursts. The dust-reddening model includes lifetime of stellar birth clouds, and the optical depths seen by stars younger and older than the clouds. They also allow four dust emission components – a Polycyclic Aromatic Hydrocarbon (PAH) template and an MIR hot dust continuum plus warm and cold dust in thermal equilibrium. Since our intent here is to test if two, simple, reddened AGN templates can fit our optical/MIR data, we shall also restrict ourselves to using two basic SFG templates with the same, simple, dust-reddening model to act as reference points. Therefore, we next describe our AGN and SFG templates and our dust-reddening model.

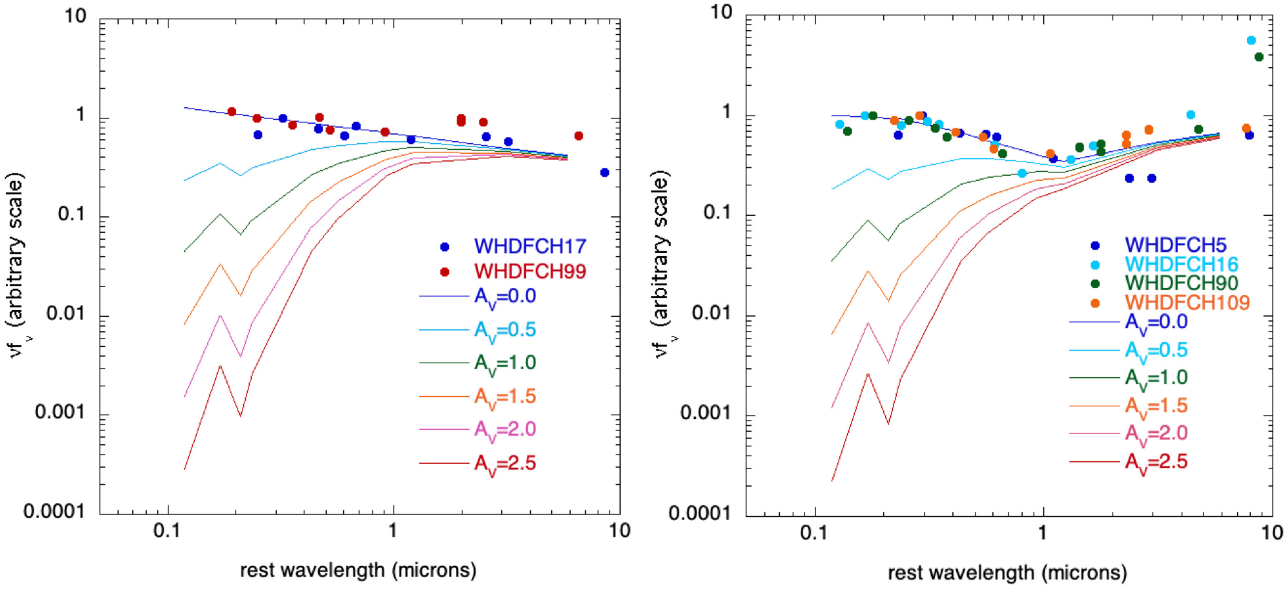

Figure 5. Single power-law and 1.4-μm 'Dip' fits to unobscured WHDF QSO SEDs to provide quasar model templates for SMG SED fitting. Also shown are the templates after application of our dust absorption model with $0 < A_V < 2.5$ mag (see Section 4.3).

4.1 AGN model SEDs

4.1.1 Single power-law AGN template

We first show the SEDs of the X-ray quasars WHDFCH017 at $z = 0.40$ and WHDFCH099 at $z = 0.82$ from the lists of Vallbe Mumbru (2004) and Bielby et al. (2012). Both have accurate *Chandra* X-ray positions, which matches to a UVX quasar. These quasars were chosen because they have a flat optical/IR spectrum in $\nu f(\nu)$ typical of about half the bright, broad-lined quasars in the WHDF. WHDFCH017, −099 have no sub-millimetre detection. The single power-law model fitted to their suitably normalized optical-MIR SEDs is:

$$\log(\nu f_\nu(\lambda)) \propto -0.28\log(\lambda) - 0.70 \quad (1)$$

as shown in Fig. 5. Here, λ is the rest wavelength in microns.

4.1.2 '1.4-μm Dip' AGN template

A further quasar template was fitted when it was realized that there were other WHDF quasars for which a power law with a 'dip' at $\approx$1 μm was a much better fit to unabsorbed X-ray QSO data. This can be seen in Fig. 5 where four WHDF QSOs, WHDFCH005, −016, −090, and −109 SEDs, are shown, after suitable re-scaling in the vertical direction. This $\approx$1-μm feature, here actually fitted at 1.44 μm, is interpreted as the break between the UV bump due to the accretion disc and the longer wavelength hot ($T \approx 300-1000$ K) dust blackbody components in QSO spectra (e.g.Richards et al. 2003; Landt et al. 2011). It is not known why other QSOs such as WHDFCH17/WHDFCH099 do not show this feature. This '1.4-μm Dip' AGN template is represented here by power-law fits in the ranges shown:

$$\log(\nu f_\nu(\lambda)) \propto -0.11\log(\lambda) - 0.10, \quad (\lambda < 0.27\mu m) \quad (2)$$

$$\log(\nu f_\nu(\lambda)) \propto -0.65\log(\lambda) - 0.41, \quad (0.27 < \lambda < 1.44\mu m) \quad (3)$$

$$\log(\nu f_\nu(\lambda)) \propto 0.72\log(\lambda) - 0.62, \quad (1.44 < \lambda < 4.32\mu m) \quad (4)$$

$$\log(\nu f_\nu(\lambda)) \propto -0.11\log(\lambda) - 0.10, \quad (\lambda > 4.32\mu m). \quad (5)$$

Both AGN models simply take a fixed 25 per cent of the flux above 0.1216 μm as representing the effect of the Lyman α forest on the SED below that wavelength.

4.2 Star-forming galaxy model SEDs

4.2.1 LAB-06 star-forming galaxy template

Although this LABOCA source has no ALMA data, it is such a bright ($r = 16.05$ mag) spiral galaxy ($z = 0.046$) that it is the unambiguous counterpart of the sub-millimetre source. The position of the galaxy is 5.″0 away from the LABOCA position, well within the 11.″3 tolerance listed in table 1 of Bielby et al. (2012). It is therefore a typical Sab spiral at the knee of the galaxy luminosity function, M^*. The fitted SED is shown in Fig. 6. In Table 1, we then see that this galaxy is detected in Herschel and VLA and in *Chandra* X-ray at the optical position. The SED is fitted by a quadratic plus a power law:

$$\log(\nu f_\nu(\lambda)) \propto -3.27\log(\lambda)^2 + 0.24\log(\lambda) - 0.92 \ (\lambda < 4.4\mu m) \quad (6)$$

$$\log(\nu f_\nu(\lambda)) \propto 0.29\log(\lambda) - 0.48 \quad (\lambda > 4.4\mu m). \quad (7)$$

4.2.2 AS2UDS star-forming galaxy template

Our other SFG model was made by taking the median SFG fit from the $\approx$700 sub-millimetre sources of Dudzevičiūtė et al. (2020) in the AS2UDS survey. Here, we fitted a quadratic plus linear model over the full optical NIR range as shown in Fig. 6. The fit to the Dudzevičiūtė et al. (2020) median AS2UDS λf_λ in their fig. 8 (left) is:

$$\log(\nu f_\nu(\lambda)) \propto 0.79 + 0.27\log(\lambda) - 2.09\log(\lambda)^2 \ (\lambda < 3.78\mu m) \quad (8)$$

$$\log(\nu f_\nu(\lambda)) \propto -0.50 + 1.28\log(\lambda) \ \ (\lambda > 3.78\mu m). \quad (9)$$

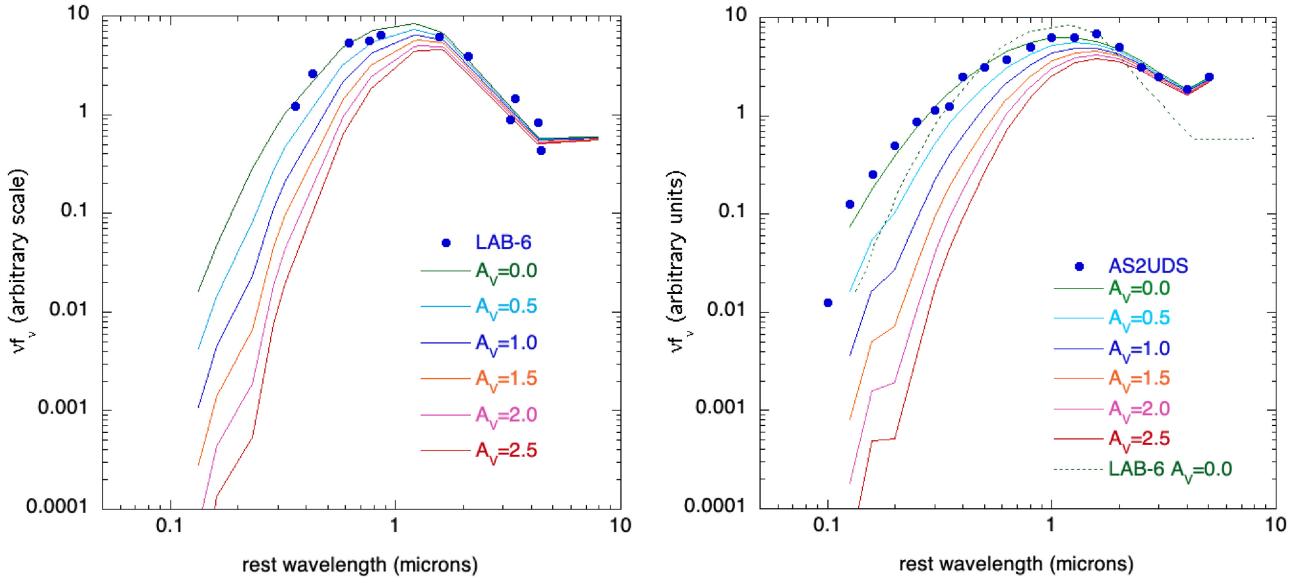

Figure 6. Fits to the LAB-06 spiral galaxy and the median AS2UDS SMG SED of Dudzevičiūtė et al. (2020) to provide the star-forming galaxy model templates for SMG SED fitting. In the right-hand panel, for comparison with AS2UDS, the green dotted line shows the LAB-06 template. Also shown are the templates after application of our dust absorption model with $0 < A_V < 2.5$ mag (see Section 4.3).

To this we applied the dust-reddening formula described in Section 4.3. As noted above, Dudzevičiūtė et al. (2020) found that with sufficient parameters, it was possible to get very good fits to their data. There are also possible flaws to our approach in that we have allowed only dust absorption to be applied to the median template and so the unabsorbed template represents the bluest model that we can fit. However, our only aim is to see how close the AGN models can get to the quality of fit of the star-forming models and this justifies our approach of minimizing the number of model parameters for both AGN and SFG templates. So, in cases where the AGN models give poor fits, the SFG templates can still give useful reference points to see how well these basic models do in comparison.

4.3 Dust-reddening law

We shall now proceed to apply a simplified dust absorption/reddening law. The reddening law is a fit to the average Milky Way reddening curve data ($R_V = 3.1$) taken from fig. 10 of Gordon et al. (2003), following Cardelli, Clayton & Mathis (1989) in the range $0.3 < x < 11.0$ where $x = 1/\lambda$ with wavelength, λ, measured in microns. The fit consists of two polynomials in the two wavelength sections given in equations (11) and (12). This allows us to include the 2200-Å dust absorption feature as found in the Milky Way. Other authors have found that including this feature is helpful in fitting high-redshift galaxy and AGN data (e.g. da Cunha et al. 2015). We extrapolate this fit for $x < 0.3$ (i.e. $\lambda = 3.33\,\mu$m) with equation (10), i.e. we assume a simple $1/\lambda$ law for infrared wavelengths longer than 3.33 μm, beyond the range of Cardelli et al. (1989) but assuming a slope in $A_\lambda/A_V(x)$ similar to that found by these authors between the J and K bands. Thus, in the fits shown below, A_λ is the absorption in magnitudes at wavelength $x = 1/\lambda$ and A_V is the absorption in magnitudes in the V band at 0.55 μm. The reddening law fits are therefore:

$$A_\lambda = A_V \times 0.25x \quad (x < 0.3) \tag{10}$$

$$A_\lambda = A_V(0.11 - 0.35x + 0.89x^2 - 0.31x^3 + 0.035x^4) \quad (0.3 < x < 4.6) \tag{11}$$

$$A_\lambda = A_V(16.4 - 5.28x + 0.62x^2 - 0.02x^3) \quad (4.6 < x < 11.0). \tag{12}$$

We shall now proceed to apply this dust-reddening law to the four optical-IR templates to judge the goodness of fit of each and the amount of dust reddening implied. The dust-absorbed templates are shown in Figs 5 and 6. Figs 7–10 then show the best AGN and SFG fits for all 12 sub-mm sources. Eight of the sub-millimetre sources have accurate ALMA positions LAB-01, -02, -03, -04, -05, -10, -11, and -12 and three have only less accurate LABOCA positions, LAB-07, -08, and -09 plus LAB-06.

4.4 Sub-millimetre-source SED fitting

We now discuss the likely counterparts to each of our 12 sub-mm sources and then the conclusions from the SED fits of the two AGN and two SFG templates. The main SED-fitting results can be found in Figs 7–10 and Table 2, with a graphical summary shown in Fig. 11.

4.4.1 LAB-01

In Fig. 1 and Table A2, we see that LAB-01 shows weak X-ray emission at $S_X(1.2-2\text{keV}) = 5.84^{+13.5}_{-4.18} \times 10^{-17}$ erg cm^{-2} s^{-1} and $S_X(2-7\text{keV}) = 7.42^{+10.1}_{-4.58} \times 10^{-16}$ erg cm^{-2} s^{-1} that appears to be absorbed with a column estimated as $N_H \approx 1 \times 10^{22}$cm^{-2}. Strong FIR emission from HeLMS is seen (see Table A4) similar to LAB-05 and LAB-11 although no radio emission is detected. There is a WHDF detection at $r = 25.4$, whdf5449, only 0.″15 offset from the ALMA position and also detected at b and H. There is a nearby (0.″15) *HST* i detection at $i_{vega} = 26.36 \pm 0.04$ mag which may be slightly extended but only at the ≈0.″2 level. The *HST* detection is difficult to see in Fig. 1. There is also a SPIES detection at [3.6] + [4.5] μm at 0.″25 from the ALMA source. It is classified as a galaxy in both SPIES bands with $class - star - ch1 = 0.002$ and $class - star - ch2 = 0.32$. Therefore, we take the WHDF/*HST*/SPIES sources to be the ALMA counterpart.

In Fig. 7, we see that the weak X-ray emission may be absorbed with a neutral H column estimated as $N_H \approx 1 \times 10^{22}$cm^{-2}. The

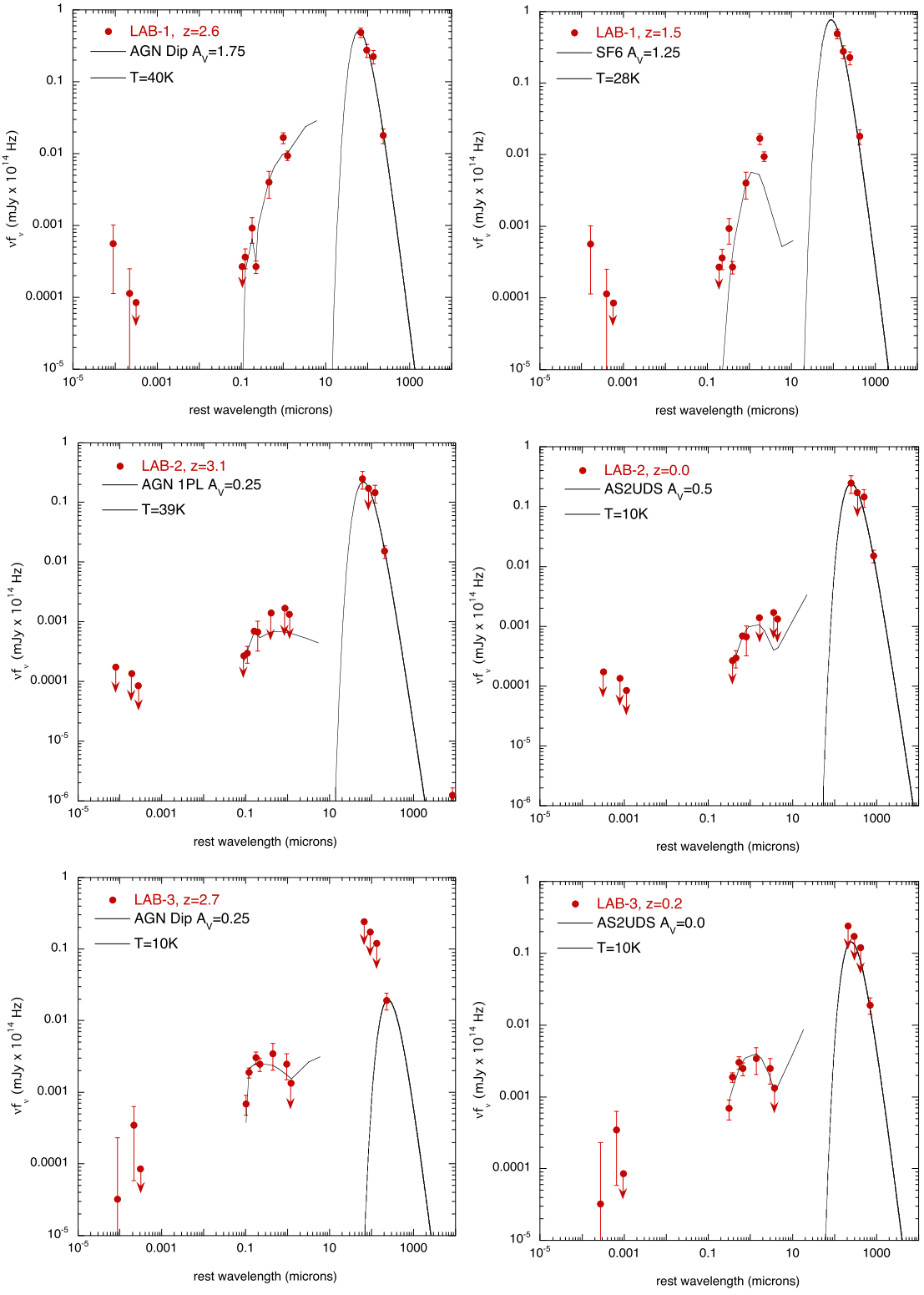

Figure 7. Comparison of LABOCA sub-millimetre sources with best-fitting quasar and star-forming galaxy templates. Note that for LAB-03, the optical/MIR detections are for a close companion since the direct counterpart is undetected in these bands. Also with only HeLMS FIR upper limits, the dust temperature (and mass) for LAB-03 are unknown and the best fit shown is therefore only nominal.

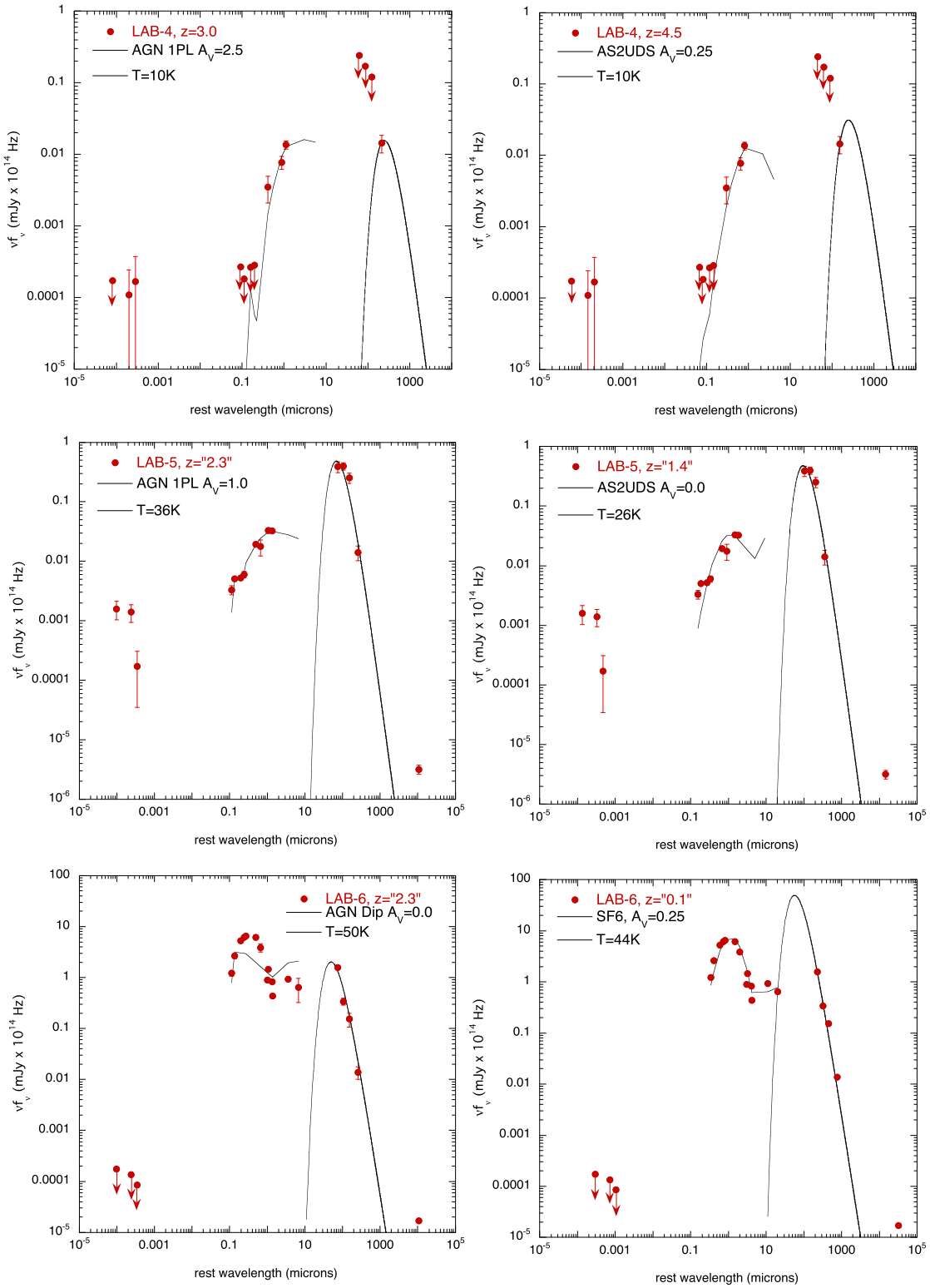

Figure 8. Comparison of LABOCA sub-millimetre sources with best-fitting quasar and star-forming galaxy templates. Note that with only HeLMS FIR upper limits, the dust temperature (and mass) for LAB-04 are unknown and the best fit shown is therefore only nominal. Also, for LAB-05, the fits are shown for the best SED-fitted redshifts, whereas its spectroscopic redshift is $z = 2.12$. The spectroscopy also identifies LAB-05 as a QSO (Bielby et al. 2012). Similarly, LAB-06 has been spectroscopically identified as $z = 0.046$ spiral galaxy and has been used here as the basis for the star-forming galaxy template, SF6.

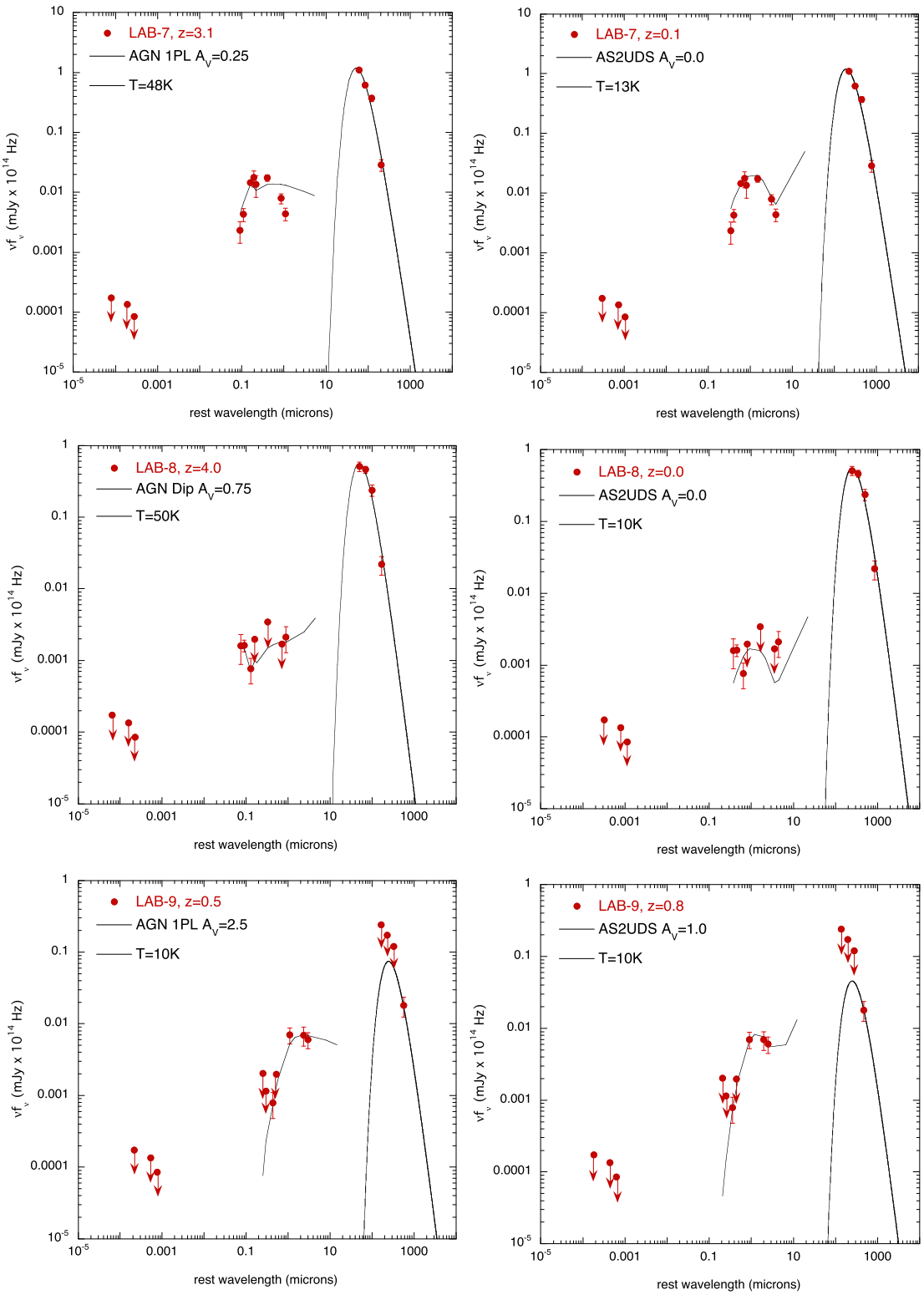

Figure 9. Comparison of LABOCA sub-millimetre sources with best-fitting quasar and star-forming galaxy templates. Note that none of these three LABOCA sources have been observed by ALMA and so their sub-millimetre positions and hence identification of counterparts are less certain than for the other sources. Also, with only HeLMS FIR upper limits, the dust temperature (and mass) for LAB-09 are unknown and the best fit shown is therefore only nominal.

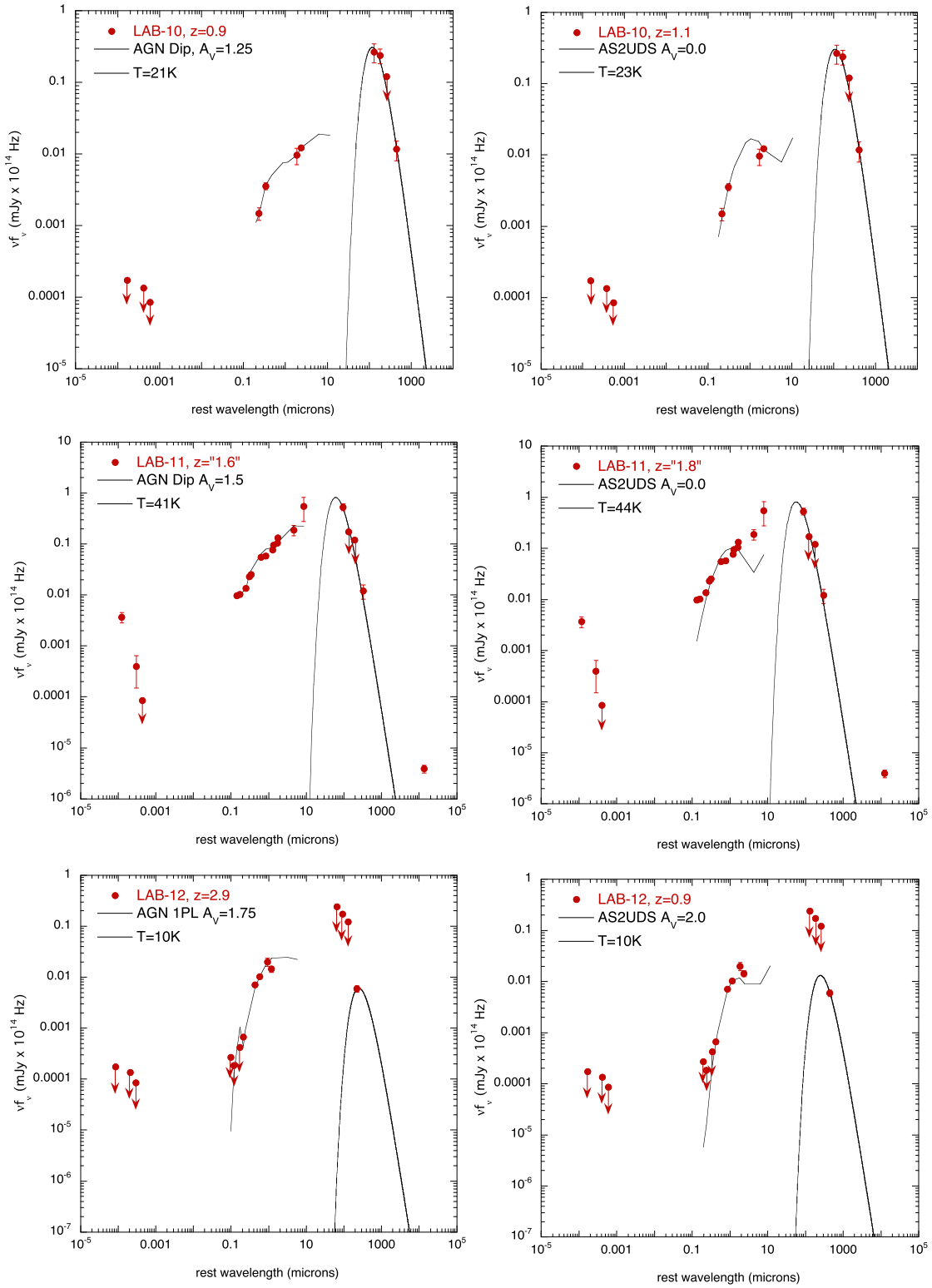

Figure 10. Comparison of LABOCA sub-millimetre sources with best-fitting quasar and star-forming galaxy templates. Note that for LAB-10, the optical/MIR detections are for a close companion since the direct counterpart is undetected in these bands. Also, for LAB-11, the fits are shown for the best SED-fitted redshifts, whereas its spectroscopic redshift is $z = 1.32$. The spectroscopy also identifies LAB-11 as a QSO (Bielby et al. 2012). Finally, with only HeLMS FIR upper limits, the dust temperature (and mass) for LAB-12 are unknown and the best fit shown is therefore only nominal.

Table 2. SED fits with parameters and errors based on maximum likelihood estimates. χ^2 values were calculated assuming these maximum likelihood parameters. "Templ" column indicates the best-fitting AGN and SFG template. In last column, *N* indicates the number of data points included in fit. For a given source, the first row refers to fit in optical/NIR/MIR and the second row refers to the fit now also including FIR detections. Temperatures and dust masses are marked n/a when they would be based only on one detected sub-millimetre flux with no other FIR fluxes except upper limits. Dust mass, M_d, is measured in solar masses assuming $\Omega_m = 0.3$, $\Omega_\Lambda = 0.7$ and Hubble parameter, $h = 1$. X-ray and radio data are excluded from fits.

	AGN + SFG template best fits												
	AGN						SFG						
LAB-	χ^2_{AGN}	T(K)	A_V(mag)	z	$M_d(M_\odot)$	Templ	χ^2_{SFG}	T(K)	A_V(mag)	z	$M_d(M_\odot)$	Templ	N
1	9.92	–	1.75 ± 0.25	2.7 ± 0.15	–	Dip	19.30	–	1.25 ± 0.38	1.5 ± 0.15	–	SF6	7
1	15.04	40 ± 6	1.75 ± 0.25	2.6 ± 0.15	2.6×10^8	Dip	24.58	28 ± 13	1.25 ± 0.38	1.5 ± 0.20	3.0×10^8	SF6	11
2	1.11	–	0.25 ± 0.38	3.1 ± 0.25	–	1PL	2.12	–	0.50 ± 0.62	0.0 ± 0.15	–	AS2	7
2	2.56	39 ± 9	0.25 ± 0.38	3.1 ± 0.25	2.0×10^8	1PL	3.56	<10	0.50 ± 0.75	0.0 ± 0.15	1.5×10^4	AS2	11
3	4.46	–	0.25 ± 0.25	3.0 ± 0.55	–	Dip	6.48	–	0.00 ± 0.12	0.1 ± 0.15	–	AS2	7
3	7.37	n/a	0.25 ± 0.25	2.7 ± 0.35	n/a	Dip	7.47	n/a	0.00 ± 0.12	0.2 ± 0.20	n/a	AS2	11
4	6.02	–	2.50 ± 0.12	3.0 ± 0.55	–	1PL	5.52	–	0.25 ± 1.00	4.5 ± 0.50	–	AS2	7
4	8.98	n/a	2.50 ± 0.25	3.0 ± 0.60	n/a	1PL	8.51	n/a	0.25 ± 1.25	4.5 ± 0.65	n/a	AS2	11
5	15.91	–	1.00 ± 0.25	2.3 ± 0.10	–	1PL	170.66	–	0.00 ± 0.12	1.4 ± 0.15	–	AS2	8
5	28.34	36 ± 5	1.00 ± 0.25	2.3 ± 0.15	3.4×10^8	1PL	182.80	26 ± 4	0.00 ± 0.12	1.4 ± 0.15	6.5×10^8	AS2	12
6	9615	–	0.00 ± 0.12	2.3 ± 0.10	–	Dip	1538	–	0.25 ± 0.25	0.1 ± 0.10	–	SF6	13
6	9654	>50	0.00 ± 0.12	2.3 ± 0.10	2.1×10^8	Dip	1543	44 ± 5	0.25 ± 0.25	0.1 ± 0.10	6.7×10^6	SF6	17
7	18.29	–	0.25 ± 0.25	3.1 ± 0.10	–	1PL	30.26	–	0.00 ± 0.12	0.1 ± 0.10	–	AS2	8
7	28.69	48 ± 3	0.25 ± 0.25	3.1 ± 0.10	3.2×10^8	1PL	41.23	13 ± 2	0.00 ± 0.12	0.1 ± 0.10	1.9×10^8	AS2	12
8	0.52	–	0.00 ± 0.25	4.0 ± 0.30	–	Dip	16.67	–	0.00 ± 0.25	0.0 ± 0.10	–	AS2	7
8	6.13	>50	0.75 ± 0.50	4.0 ± 0.20	2.2×10^8	Dip	22.15	<10	0.00 ± 0.25	0.0 ± 0.05	3.5×10^4	AS2	11
9	2.51	–	2.50 ± 0.25	0.4 ± 0.30	–	1PL	1.87	–	1.00 ± 0.62	0.8 ± 0.25	–	AS2	7
9	4.17	n/a	2.50 ± 0.38	0.5 ± 0.35	n/a	1PL	3.74	n/a	1.00 ± 0.75	0.8 ± 0.35	n/a	AS2	11
10	2.03	–	1.25 ± 0.25	0.9 ± 0.15	–	Dip	6.86	–	0.00 ± 0.12	1.1 ± 0.10	–	AS2	7
10	3.07	21 ± 8	1.25 ± 0.25	0.9 ± 0.20	4.9×10^8	Dip	7.86	23 ± 6	0.00 ± 0.12	1.1 ± 0.15	4.6×10^8	AS2	11
11	43.18	–	1.50 ± 0.25	1.6 ± 0.10	–	Dip	243.01	–	0.00 ± 0.12	1.8 ± 0.15	–	AS2	13
11	44.21	41 ± 10	1.50 ± 0.25	1.6 ± 0.10	1.1×10^8	Dip	244.02	44 ± 8	0.00 ± 0.12	1.8 ± 0.15	9.7×10^7	AS2	17
12	16.87	–	1.75 ± 0.25	2.9 ± 0.10	–	1PL	18.68	–	2.00 ± 0.25	0.9 ± 0.10	–	AS2	8
12	19.85	n/a	1.75 ± 0.25	2.9 ± 0.10	n/a	1PL	21.3	n/a	2.00 ± 0.25	0.9 ± 0.10	n/a	AS2	12

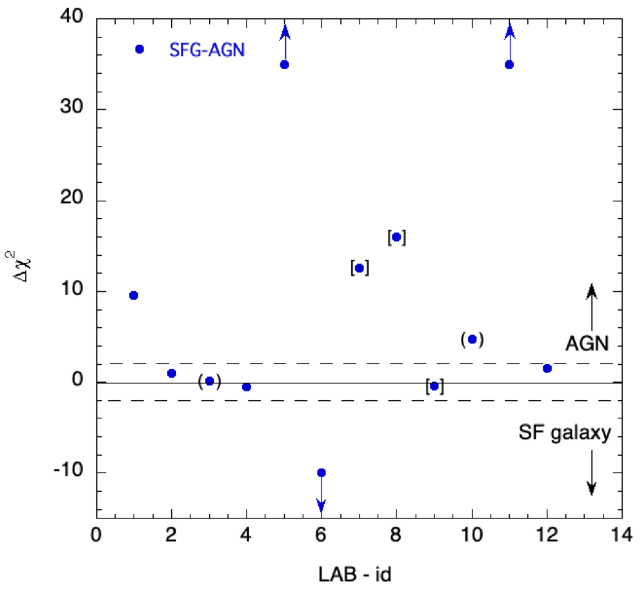

Figure 11. $\Delta\chi^2$ comparison of the best-fitting star-forming galaxy (SFG) and AGN models from the results in Table 2. LAB-03 and -10 are shown in brackets since they are believed to be companions rather than counterparts. LAB-07, -08, and -09 are shown in square brackets since these counterparts are less certain due to only having LABOCA source positions.

comparison with the best-fitting 1.4-μm dip AGN model gives a dust reddening of $A_V = 1.75 \pm 0.25$ mag and a redshift of $z = 2.6 \pm 0.15$. The fit to the star-forming galaxy is formally worse at least at the $\Delta\chi^2 = 9.54$, 4σ level for all A_V values than the AGN fits. Nevertheless, there is a suggestion that the 1.6-μm feature in the SF6 template may fit better. In the SPIES data, the 3.6-μm flux corresponds to [3.6] = 17.88 (auto,Vega) with [3.6]−[4.5] = 0.56 for aperture 1 with a 1.″44 radius, consistent with an AGN and therefore suggesting that the possible 1.6-μm feature is compatible with what is seen in QSO spectra. Conclusion: The X-ray detection suggests that it is a QSO.

4.4.2 LAB-02

In Fig. 1 and Table A2, we see that LAB-02 shows no X-ray emission. Strong FIR emission is seen as well as 8.4-GHz radio emission (see Table A4), although the radio source lies at 2.″9 from the ALMA position. The optical position (whdf9271) is also 1.″65 away and faint at $r = 25.8$. The WHDF list classifies it as 10, signifying a multiple source. But it is clearly detected on the *HST i*-band image as a point source (≈0.″2 FWHM) 0.″96 offset from whdf9271. It is also 0.″96 from the ALMA source and we consider this WHDF/*HST* source as the ALMA counterpart. A faint, 2.77×10^{-3} mJy, SPIES 4.5-μm source is detected within 1.″54 of the optical position and 2.″18 from the ALMA position. The source has $class - star - ch2 = 0.46$, midway between point source and extended. But we judged 2.″18 to be too far away to be the ALMA counterpart and so there are only SPIES [3.6], [4.5] μm upper limits assumed for this ALMA source.

In Fig. 7, the comparison with the best-fitting 1 power-law AGN model implies a dust absorption of $A_V = 0.25 \pm 0.38$ mag a redshift $z = 3.1 \pm 0.25$, and $T \approx 39$ K. The best fit to a star-forming galaxy is AS2UDS with $A_V = 0.5 \pm 0.75$ and $z = 0.0 \pm 0.15$ with a low fitted dust temperature of $T < 10$ K. The star-forming fit is marginally worse than the 1 power-law AGN model at the $\Delta\chi^2 = 1.0$ level but this rises to $\Delta\chi^2 > 9.5$ for any $z > 0.5$ whatever the A_V. The

FIR/radio ratio also suggests a high-redshift object, with the caveat about the ALMA/radio offset. Conclusion: probable QSO.

4.4.3 LAB-03

In Fig. 1 and Table A2, we see that LAB-03 shows some evidence of X-ray emission in the two harder bands $S_X(1.2-2\mathrm{keV}) = 1.77^{+2.5}_{-1.1} \times 10^{-16}$ erg cm^{-2} s^{-1} and $S_X(2-7\mathrm{keV}) = 6.29^{+4.8}_{-1.0} \times 10^{-17}$ erg cm^{-2} s^{-1} within 0.″17 of the ALMA position. We are reasonably satisfied that the WHDF source whdf9547 at $r = 24.15$ is identified with the double galaxy shown on the *HST i* (see Fig. 1) image, which is offset by 1.″82 from the ALMA position. A SPIES 3.6-μm source close to the detection limit is seen at 1.″57 offset from ALMA and 1.″24 from whdf1234. It is classified as a probable galaxy in the [3.6] μm SPIES band with $class - star - ch1 = 0.48$. This source may possibly be associated with a fainter object detected in *HST i*, offset 1.″24 NW of the double galaxy. Generally, there is significant doubt about whether any of these optical/NIR detections are directly associated with the ALMA sub-millimetre source, which is significantly offset from the WHDF (+*HST*) galaxy at a separation of ≈1.″54 and from the SPIES source at 1.″57 (see Fig. 7). We note that there is a faint object detected only in the *H* band, which may be the actual counterpart as shown in Fig. 1 at the '*H*-band' coordinate listed in Table A2.

We have therefore fitted the SED (see Fig. 7) assuming that the whdf1234, *HST*, and SPIES sources are from the double galaxy, but this object is unlikely to be the direct counterpart of the sub-millimetre source and more likely to be a companion. The SED best fit is the 1.4-μm dip AGN model with $z = 2.7 \pm 0.35$ and $A_V = 0.25 \pm 0.25$, $T < 10$ K, but the AS2UDS star-forming fit with $z = 0.2$, $A_V = 0.0$, and $T < 10$ K is only negligibly worse ($\Delta\chi^2 = 0.1$). In the SPIES data, [3.6] = 19.49 (automag Vega) and it is undetected in the [4.5] band. The upper limit on the [4.5] flux gives [3.6]−[4.5] < 0.31 for aperture 1. Here, because of the uncertainty of the optical/NIR counterpart, we weight the detection of the weak X-ray source at the exact ALMA position more highly and conclude that LAB-03 is an obscured quasar possibly associated indirectly with the object at $z \approx 2.7$, again bearing in mind the caveats about the uncertain optical/NIR counterpart. Conclusion: QSO.

4.4.4 LAB-04

This is the archetypal SMG in the WHDF with no *UBRI* detections and only detections at *H*, [3.6] and [4.5]. However, the *H* and SPIES detections are relatively strong and are both within the 0.″25−0.″5 range. There is also a hint of X-ray detection in the two softer bands at $S_X(0.5-1.2\mathrm{keV}) = 1.09^{+2.5}_{-0.78} \times 10^{-16}$ erg cm^{-2} s^{-1} and $S_X(1.2-2\mathrm{keV}) = 2.28^{+1.3}_{-0.4} \times 10^{-16}$ erg cm^{-2} s$^{-1,}$ although none in the harder band. The X-ray source is within 0.″095 of the ALMA position. In the SPIES data, LAB-04 is detected in both bands with [3.6] = 18.72 (automag Vega) and with [3.6]−[4.5] = 1.03 Vega in ap1. It is also classified as a star in the [3.6] band with $class - star - ch1 = 0.62$ and as a galaxy in the [4.5] band with $class - star - ch2 = 0.21$.

From the SEDs in Fig. 8, it is difficult to rule out either an AGN or SF origin for LAB-04 although there is a marginal $\Delta\chi^2 = 0.47$ preference for a $z = 4.5$, $A_V = 0.25$ AS2UDS SFG template over the $z = 3.0$, $A_V = 2.5$, 1 power-law AGN. However, the [3.6]−[4.5] = 1.03 colour satisfies the [3.6]−[4.5] > 0.4 criterion for a quasar. We recall that even with $A_V = 10$ mag, $A_{3.6} = 1.53$, $A_{4.5} = 1.22$ mag ,the colour would be affected only by 0.31 mag, keeping the colour well into the QSO range. On the basis of the X-ray detection and SPIES colour: Conclusion: QSO.

4.4.5 LAB-05

LAB-05 has been previously identified showing strong X-ray emission ($S_X(0.5-1.2\mathrm{keV}) = 1.11^{+1.5}_{-0.68} \times 10^{-16}$ erg cm^{-2} s^{-1}, $S_X(1.2-2\mathrm{keV}) = 7.18^{+3.4}_{-2.4} \times 10^{-16}$ erg cm^{-2} s^{-1}, and $S_X(2-7\mathrm{keV}) = 2.09^{+1.1}_{-0.74} \times 10^{-15}$ erg cm^{-2} s^{-1}) that appears to be absorbed with a column estimated as $N_H \approx 1 \times 10^{23}$cm^{-2} (Bielby et al. 2012, following Vallbe Mumbru 2004). This is confirmed with the X-ray source being only offset from the ALMA position by 0.″38. Strong FIR emission is seen as well as 8.4-GHz radio emission, although the radio source EVLA-8 is offset by 1.″40 from the ALMA position. The closest WHDF counterpart is whdf6483, offset from ALMA by 0.″56 (see Fig. 1 and Table A2) and is classified as a galaxy in the WHDF *r*-band. This object is UVX and has spectroscopic confirmation as a $z = 2.12$ narrow-lined QSO, WHDFCH008 from Bielby et al. (2012). Now the offset between whdf6483 and the X-ray position is 0.″65, but we take these to be the same object and the counterpart to the LAB-05 ALMA source. There is also a SPIES [3.6], [4.5] detection at 0.″31 offset from the ALMA source (see Fig. 1). It is also classified as a galaxy in both SPIES bands with $class - star - ch1 = 0.23$ and $class - star - ch2 = 0.07$.

The SED comparison with the best-fit single power-law AGN model in Fig. 8 gives a dust absorption of $A_V = 1.0 \pm 0.25$ mag. The comparison with the best-fitting 1 power-law AGN model gives a dust absorption of $A_V \approx 1.25 \pm 0.1$ mag. Both give $z = 2.3 \pm 0.15$, consistent with the actual redshift of $z = 2.12$. We note that the reduced χ^2 of the overall best-fitting 1.4-μm dip AGN model is 4.04 mainly due to a large residual on the *u*-band data at rest wavelength of 0.1 μm. We decided against any increase of the empirical error to provide a smaller χ^2, so we shall bear in mind that the AGN models are not perfect fits to this known QSO. The fit to the star-forming galaxy is very significantly worse for all A_V values (see Table 2 and Fig. 11). We further note that the AGN absorption of $A_V = 1.25$ can be compared to $A_V \approx 45$ mag implied by the X-ray absorption suggesting that the X-ray absorption is located at closer line-of-sight distance to the QSO where dust may be destroyed, with the dust that we measure via the SED lying further away. In the SPIES data, [3.6] = 17.15 (Vega) with [3.6]−[4.5] = 0.96 for aperture-1. Conclusion: $z = 2.12$ QSO.

4.4.6 LAB-06

Although this LABOCA source has no ALMA data, it is such a bright ($r = 16.07$ mag) spiral galaxy ($z = 0.046$) that it is the unambiguous counterpart of the sub-millimetre sources. The position of the galaxy (whdf3406) is 5.″0 away from the LABOCA position, well within the the 11.″3 tolerance listed in table 1 of Bielby et al. (2012). It is therefore a typical Sab spiral at the knee of the galaxy luminosity function, M^*. In Fig. 8, we then see that this galaxy is detected in Herschel, VLA, and *Chandra* X-ray, the latter at a faint flux of $S_X(1.2-2\,\mathrm{keV}) \approx 6.8 \times 10^{-17}$ erg cm^{-2} s^{-1} at the optical position. We have already noted our use of this sub-millimetre galaxy as one of our two templates for a dusty SFG. Conclusion:$z = 0.046$ spiral galaxy.

4.4.7 LAB-07

Here, we have LABOCA data but no ALMA data. The uncertainty on the position is $\Delta\theta = 11.''6$ according to Bielby et al. (2012). There are three possible optical sources associated with three SPIES sources at $8.''0$ (LAB-07-1), $4.''5$ (LAB-07-2), and $3.''0$ (LAB-07-3) offsets (see Fig. 2). The faintest optical/SPIES source at the largest offset is also a very faint ($\approx 1\sigma$) X-ray source in the two harder bands. But since this is below our X-ray significance threshold and since the brightest optical/SPIES source (LAB-07-3) is also the closest to the LABOCA position and also has a low-significance X-ray detection, we consider this source (whdfext3652) as the most likely counterpart. This source is classified morphologically as a galaxy in SPIES and in WHDF. LAB-07 is also close to a strong Herschel source at 250, 350, and 500 μm (see Table A4).

In terms of SED fitting, both AGN fits give $z = 3.1 \pm 0.1$, $A_V = 0.0 \pm 0.1$, and $T = 48$ K, and are significantly better than either of the SFG fits with SF6, giving the best fit with $z = 0.1$, $A_V = 0.0$, and $T = 13$K. Moreover, the AS2UDS SED fits both strongly reject redshifts $z > 0.5$. Also, the SPIES data give $[3.6] = 18.69$ with $[3.6]-[4.5] = 0.49$ for aperture-1. Again, this seems not to fit with a low-redshift galaxy. Although there is uncertainty in the counterpart, the better AGN fit, low-significance X-ray detection, and red SPIES colour suggest a QSO. Conclusion: Probable QSO

4.4.8 LAB-08

Again, we have LABOCA but no ALMA data. The uncertainty on the LABOCA position is $\Delta\theta = 12.''6$ according to Bielby et al. (2012). No X-rays nor radio emission are detected. The optical source whdfext3250 is faint at $r = 25.6$ and lies at $4''.2$ E, $0.''8$ N from the LABOCA coordinate (see Fig. 2). Two very low S/N SPIES 3.6-μm sources and one similarly low S/N 4.5-μm source are detected but all at slightly larger distances ($4.''7$, $5.''8$, and $7.''6$) from the LABOCA position than whdfext3250. However, a second faint 4.5-μm source is detected at higher S/N closer to the whdfext3250 position ($2.''8$ E, $2.''07$ N). We therefore take whdfext3250 as the counterpart $4.''3$ from the LABOCA position as this is the closest candidate, together with this [4.5] μm source, despite these larger than usual offsets between the optical and the [4.5] μm positions. Morphologically, whdfext3250 is identified as a galaxy in the r band and the 4.5-μm band. Although not detected at 3.6 μm, whdfext3250 is strongly detected in the u band and is formally UVX at $u - b = -0.67 \pm 0.2$. LAB-08 is also close to a strong Herschel HeLMS source at 250, 350, and 500 μm.

The AGN SED fits are both much better than the SFG fits with the best 1 power-law AGN model with $z = 4.0 \pm 0.2$, $A_V = 0.75 \pm 0.5$ nd $T > 50$ K having $\Delta\chi^2 = 16.02$ over the best AS2UDS fit with $z \approx 0.0$, $A_V \approx 0.0$ and $T > 50$ K. However, it has to be said that both best fits are unconvincing in Fig. 9 and both give $z = 0.0$ (see Table 2). The lack of a detection in 3.6-μm band gives a lower limit of $[3.6]-[4.5] > 0.80$, which is again consistent with a QSO. This and its UVX property suggest a QSO, but there is still uncertainty over whether it is the counterpart. Conclusion: Probable QSO.

4.4.9 LAB-09

Again, we have LABOCA but no ALMA data. Neither VLA radio emission nor Herschel FIR emission is detected. Only a weak X-ray source in the softest and hardest bands may be detected at the LABOCA position but these are not even jointly significant at 1σ. A faint optical/IR source (whdfext5230) with $r = 25.6$ and $H = 21.05$ is detected within $2''$ of the LABOCA position. whdfext5230 is coincident with a source detected in SPIES at 3.6 and 4.5 μm (see Fig. 2 and Table A3). The [3.6]–[4.5] = 0.44 colour is above the 0.4-mag threshold for a QSO. With *class* – *star* – *ch*1 = 0.407 and *class* – *star* – *ch*2 = 0.117, both correspond to galaxies and similarly for the r-band morphology.

The best overall SED fit is given by the AS2UDS SFG model with $z = 0.8 \pm 0.35$, $A_V = 1.0 \pm 0.75$, and formally $T < 10$ K, but with three upper limits from HeLMS, there is essentially no constraint on the dust temperature. However, the $\Delta\chi^2 = 0.43$ is only a marginal advantage for the AS2UDS template over the single power-law AGN template, which also gives a low redshift ($z = 0.5 \pm 0.35$). However, a $z \approx 0.5$ QSO is more consistent with the SPIES colour than a $z \approx 0.8$ galaxy. Although the counterpart is also uncertain, we therefore conclude that this source is a probable QSO. Conclusion: Probable QSO.

4.4.10 LAB-10

This source has ALMA data as well as LABOCA data. We note that it lies in the outskirts of a nearby early-type galaxy and this makes detection more difficult in the optical bands. Neither radio nor X-ray emission is detected. Herschel FIR emission is detected at 250 and 350 μm. An optical source, whdf428 is detected at $r = 23.97$ and $b = 25.62$, offset by $1.''68$ from the ALMA position (see Fig. 1 and Table A3). A point-like source is also detected on the *HSTi* frame, $1.''2$ West of the ALMA source at $i = 25.85 \pm 0.05$, and mid-way to the WHDF source with a further $1.''2$ offset, and is probably the counterpart to whdf428. A source is also detected quite strongly at 3.6 and 4.5 μm in SPIES at $1.''9$ offset from the ALMA source. This SPIES source is probably the *HST* diffuse source to the SW of the *HST* point source. Although the *HST* point source could be the counterpart of whdf428 and the SPIES source, we regard the $1.''2$ offset of the *HST* point source from the ALMA source as too far for it to be its counterpart. Although the offsets for optical and SPIES sources are $>1''.0$, we treat these as the detected components of a single object, given the possible astrometric errors. We therefore treat whdf428 as a companion to the ALMA source rather than its direct counterpart. In SED fitting, we quickly found that the *HST i* = 25.85 mag was too faint for continuity with the brighter whdf428 and SPIES magnitudes, so this was eliminated from the analysis, implying that it may only be a second, closer, companion to the ALMA source. Thus, for the other whdf428+SPIES companion, we find that in both SPIES bands, whdf428 is classed as a galaxy (*class* – *star* – 1, −2 = 0.0) and similarly in r (SG = 5). The SPIES colour is $[3.6]-[4.5] = 0.92$, well into the QSO locus.

The best SED fit for whdf428 (see Fig. 10) is given by the AGN 1.4-μm 'Dip' model with $z = 0.9$, $A_V = 1.25$, and $T = 21$K with $\Delta\chi^2 = 4.8$ compared to the best-fitting AS2UDS star-forming model (see Fig. 11 and Table 2). We conclude that although the SPIES colour suggests that whdf428 is a QSO, its $2.''3$ offset from the ALMA source makes it unlikely to be the counterpart. The $i = 25.85$ mag *HST* detection may still possibly be the counterpart but that object is detected only in that band. Conclusion: Unknown.

4.4.11 LAB-11

This is a known QSO, WHDFCH007, with $z = 1.32$ (Bielby et al. 2012). In Fig. 1 and Table A2, we see that LAB-11 shows strong X-ray emission in the two harder bands ($S_X(1.2-2\text{keV}) = 2.02^{+2.0}_{-1.1} \times 10^{-16}$ erg cm^{-2} s^{-1} and $S_X(2-7\text{keV}) = 4.81^{+1.6}_{-1.2} \times 10^{-15}$ erg cm^{-2}

s^{-1}) that appears to be absorbed with a column estimated as $N_H \approx 5 \times 10^{23} cm^{-2}$ (Bielby et al. 2012). Strong FIR emission is seen as well as 8.4-GHz radio emission. The closest WHDF detection, whdf6423, is offset 0.″5 from the ALMA source. The *HST* detection is offset 0.″18 from ALMA and 0.″60 from whdf6423. The only discrepancy is that the VLA detection is 1.″23 offset from ALMA. It is classed as a galaxy in the [3.6] band with $class - star - ch1 = 0.21$ and a star in the [4.5] band with $class - star - ch2 = 0.88$. In the SPIES data, [3.6] = 15.99 (automag Vega) with [3.6]−[4.5] = 1.08 for aperture 1 with a 1.″44 radius.

The SED fit for the 1.4-μm dip AGN model (see Fig. 10) gives $A_V = 1.5 \pm 0.1$ mag and $z = 1.6 \pm 0.1$, and $T = 32 \pm 5$K. The fit to the AGN 1 power-law model is worse although giving similar parameter values. The fits to the star-forming galaxies are very significantly worse for all A_V values. Conclusion: $z = 1.32$ QSO.

4.4.12 LAB-12

This object was picked up in the same ALMA observation as for LAB-11. It is ≈2× fainter at 870 μm than LAB-11 and lying 10.″6 SE. It is in the direction of a second 8.4-GHz radio peak detected in EVLA-6 (see fig. 2 of Heywood et al. 2013), now called EVLA-6-2, but EVLA-6-2 is a further 4.″05 ± 0.″75 E and 4.″91 ± 1.″91 S of LAB-12 (see Table A4), suggesting EVLA-6-2 is not a radio counterpart of LAB-12. No X-rays were detected from this sub-millimetre source. There is also no WHDF optical detection but a faint source is detected in the *HST i* band at 0.″43 offset from the ALMA source with $i_{Vega} = 25.38 \pm 0.04$. It is also strongly detected in the *H*, *K* bands at 0.″32 offset with $H = 21.04 \pm 0.02$ and $K = 19.87 \pm 0.02$. In SPIES, the nearest and brightest source was first thought to be detected only in the 4.5-μm band at 0.″24 from the ALMA source with the nearest 3.6-μm source 1.″68 away. However, inspection of the 3.6-μm image indicates that the source detected there should have the same coordinates as the 4.5-μm sources. We then find [3.6] = 17.69 (Vega auto) and [3.6]−[4.5] = 1.43 (ap1 Vega). Again, this is well into the QSO locus.

The best SED fit is given by the AGN 1.4-μm dip model with $\Delta\chi^2 = 2.07$ over the AS2UDS star-forming template. Both models fit reasonably well with $\chi^2 = 19.27$ for the AGN model and $\chi^2 = 21.34$ for the AS2UDS template with 7df. Conclusion: Probable QSO

4.5 SED-fitting results summary

We have seen that the AGN models fit the SMG SEDs at least as well as the SFG templates where the counterparts can be identified (see Fig. 11). The main exception is the nearby spiral galaxy LAB-06. Of course, with a larger selection of star-forming templates arbitrarily good fits to most SMG SEDs can be obtained as shown by Dudzevičiūtė et al. (2020); clearly with enough model components, increasingly good fits can be expected. Here, we have therefore fitted only two simple SFG templates, one based on LAB-06 and one based on the median SMG fit of Dudzevičiūtė et al. (2020), to make a fair comparison to the two simple AGN templates we have employed, while keeping the number of model components low. We also caution that the counterparts to LAB-03, -10 are unknown despite having accurate ALMA positions and are thus bracketted in Fig. 11 due to close companions having had their SEDs fitted in these two cases. Similarly, the counterparts to LAB-07, -08, and -09 are enclosed in square brackets in Fig. 11 due to the uncertainty in the identity of their counterparts due to their having only LABOCA source positions.

One possible issue is that we have not allowed lower dust absorption than set by the median star-forming template, so in cases where the best star-forming fit has $A_V = 0.0$, i.e. LAB-03, -05, -07, -08, and -11, this might bias the AGN-SF comparison. But LAB-05, -11 are previously identified X-ray QSOs and LAB-03 also shows weak X-ray emission. So only the LABOCA sources LAB-07, -08 are left as being possibly subject to this bias and none of the ALMA targets. Even LAB-07, -08 are fitted at $z \approx 0$, which is unlikely for luminous sub-millimetre sources. The star-forming fits also put LAB-02 and LAB-03 at implausibly low redshifts.

A summary of the best AGN and SFG template fits for each sub-millimetre source is given in Table 2, listing the best-fitting values for the redshift, dust temperature, *T*, dust mass, M_d, and visual absorption, A_V. The 11 AGN redshifts (excluding the SFG LAB-06) range from $0 < z < 4.5$ with an average $z = 2.43 \pm 0.31$, and the absorptions range from $0 < A_V < 2.5$ mag with an average of $A_V = 1.25 \pm 0.25$ mag. With many SFG fits being skewed to $z = 0$, we do not quote averages for these. We also do not quote average absorption for the SFG fits because recall that they do not include the extra absorption in the original templates. For the AGN FIR fits that have more than one FIR data point and again excluding LAB-06, we find that the dust mass ranges between $1.1 < M_d < 4.9 \times 10^8 M_\odot$ with an average of $M_d = 1.77 \pm 0.46 \times 10^8 M_\odot$. The dust temperatures for these seven (including the LAB-08 lower limit of 50 K) range from $21 < T < 50$ K with an average $T = 39.3 \pm 3.6$ K. The ranges of M_d for the SFG fits are much wider and if necessary can be obtained from Table 2. These ranges and averages for redshift, absorption, dust temperature, and dust mass are quite consistent with those found in other sub-millimetre source studies where more quasar spectroscopic redshifts are available.

5 DISCUSSION

We have compared SED fits of AGN and star-forming templates to a complete sample of 12 sub-mm sources in the WHDF over the optical-MIR and FIR wavelengths. *Chandra* X-ray data were also available for several sources but not fitted. Eight of the 12 sources originally identified by LABOCA have high-resolution, high S/N ALMA data. Of the two AGN templates we used, we find that about half are better fitted by a single power-law model and the other half by a model with a minimum or 'dip' at 1.4 μm. This 'dip' represents the split between the 'blue bump' from the accretion disc at shorter wavelengths and hot dust components at longer wavelengths. For the star-forming templates, we used an empirical template from the $z = 0.046$ spiral galaxy, LAB-06, that is one of our 12 sub-mm sources. We also used a template fitted from the median best-fitting SMG SED fitted by Dudzevičiūtė et al. (2020) to ≈700 AS2UDS sub-millimetre sources. Here, we found that the AS2UDS template was the better star-forming fit to 10/12 WHDF sub-millimetre sources.

In the comparison between the best AGN and star-forming template fits, we found that the AGN template fitted better in five cases (LAB-01, -05, -07, -08, and -11) and in the star-forming template in one case (LAB-06), there was no significant difference at 2σ in four cases (LAB-02, -04, -09, and -12), and the optical/NIR/MIR counterpart was unidentified in two cases (LAB-03, -10). The main fitted parameters were the dust extinction A_V in the optical-NIR, the dust temperature in the FIR, and the redshift jointly between the two. We re-iterate that there is increased uncertainty about the counterparts of the LABOCA-only sources, LAB-07, -08, and -09, given the lower precision in their sub-millimetre source positions.

The X-ray data provided further important constraints. Two sub-millimetre sources, LAB-5 and LAB-11, had already been identified as absorbed X-ray quasars by Bielby et al. (2012) from the 3σ X-

ray catalogue of Vallbe Mumbru (2004). With the help of the ALMA data, a re-inspection of the X-ray data found traces of low S/N X-rays in the case of three further sub-millimetre sources, LAB-01, -03, and -04. For LAB-01 and LAB-04, the fitted redshifts place their X-ray luminosity at $L_X > 10^{42}$ erg s^{-1} implying that they are quasars. The detection of X-rays in the sub-millimetre source LAB-03 increases the probability that it is a quasar although we note that the doubt about its counterpart leaves its redshift uncertain. The X-ray identifications of LAB-01, LAB-03, and LAB-04 as quasars leaves 7 sub-mm sources identified as quasars (LAB-01, -03, -04, -05, -07, -08, and -11), three (LAB-02, -09, and -12) with no preference between AGN and star-forming template at 2σ, one low-redshift star-forming spiral (LAB-06), and two with no optical/IR/X-ray counterpart identified (LAB-10).

We conclude that AGN make at least as good fits to 10/12 or 83 ± 26 per cent of sub-millimetre sources with only one source (≈8 per cent) where an SFG was clearly the better fit, the $z = 0.046$ spiral galaxy, LAB-06. We have also noted that the majority of these 10 sources have $W1-W2 > 0.4$ consistent with them being quasars. We acknowledge that other authors have also found excellent fits to SMG SEDs with pure star-forming templates and, given our results, we expect that models with a mixture of AGN and star-forming templates should also provide good fits (e.g. Wang et al. in preparation). We again emphasize that the minimum AGN fraction of the 8 with ALMA positions comprises those with X-ray detections, i.e. LAB-01, LAB-03, LAB-04, LAB-05, and LAB-11, i.e. 5/8 or 62.5 per cent. One further caveat to be made is that we have little data at 8–100 μm between the SPIES and Herschel/LABOCA/ALMA wavelengths. It has been previously suggested that hot dust at observed wavelengths of 5–24 μm differentiates quasars from other SMGs, although they are indistinguishable in the 250-, 350-, 500-μm band colours (e.g. fig. 1 of Hatziminaoglou et al. 2010). We have argued that the 3.6-, 4.5-, 5.5-, and 8-μm colours of SMGs showing the same colours as quasars in fig. 2(c) of Dudzevičiūtė et al. (2020) sample of ≈700 SMGs imply that differences in the hottest dust component may not be significant between the two populations.

Hill & Shanks (2011a) argued that X-ray-absorbed quasars may be more likely to show FIR emission based on LAB-05, LAB-11. They built a model where more X-ray-absorbed quasars had more dust emission that could explain ≈ 50 per cent of the sub-millimetre background with a further 50 per cent arising from faint SFGs. However, this model is not unified – in the case of the simplest models, face-on nuclei with little HI column might be expected to show similar amounts of FIR dust emission as edge-on-oriented quasar discs showing significantly larger HI column. But the Hill & Shanks model would imply more dust emission in the latter case. Also, such a model may not explain the Hatziminaoglou et al. (2010) results unless there were distinct AGN populations with either hot or cold dust components.

We therefore now consider such an adjustment to the Hill & Shanks model where intrinsically brighter quasars show more hot dust emission than fainter AGN. This is supported by our finding that our X-ray quasar sample is, on the average, ≈10× brighter at 3.6–4.5 μm than our LABOCA/ALMA sub-millimetre sample (see Fig. 3). Certainly, the small amounts of dust extinction ($A_V <$ 2.5 mag) seen in our SED fits are not enough to account for the sub-luminous 3.6–4.5 μm emission of SMGs. An anticorrelation between MIR and FIR luminosities where dust is heated and/or destroyed in the environment of the brightest quasars could easily explain the Hatziminaoglou et al. (2010) result. Such a correlation has also been seen in other X-ray-selected AGN by Ricci et al. (2017), at least in the form of X-ray quasars with high Eddington ratios having lower X-ray absorption columns. This result can be interpreted as, for a fixed M_{BH}, higher luminosity quasars have less dusty gas due to heating by quasar outflows.

The sub-millimetre counts at >1 mJy can then be explained by intrinsically fainter, X-ray-absorbed quasars at L_X^*, while the sub-mJy counts would still be explained by modetly star-forming galaxies like the spiral LAB-06. In the L_X^* quasar population both hot ≈300−1000 K dust at a few parsecs radius from the accretion disc and cooler ≈35 K dust at ≈1 kpc would be found. At this latter distance, PAH features could survive the X-rays from the quasar nucleus and so the presence of these features would no longer present a difficulty for a model with AGN heating (e.g. Veilleux et al. 2009). This revised model would still retain the main feature of the Hill & Shanks (2011a) model, i.e. that AGN are, in the main, responsible for both the sub-millimetre and X-ray backgrounds.

The fainter MIR luminosities of SMGs could still be consistent with dust heating being more due to star formation if their low MIR luminosity simply indicated that they were more like galaxies than AGN. However, the SMG bolometric luminosity still reaches the quasar level when the cold dust component is included, so it seems more natural if they were AGN dominated.

We shall see in Paper II that the size of the ALMA cold dust sources here is ≈1 kpc, consistent with the prediction from the AGN-heated model. Also, at these small sizes, we shall find that the SMGs are closer to the SFR surface brightness Eddington ratio compared to the AGN Eddington ratio.

6 CONCLUSIONS

We have investigated the SEDs of 12 sub-mm sources in the WHDF, using multiwavelength data ranging from the X-ray to the radio. Our approach has been to focus on a small but complete sample of sub-millimetre sources observed with data of the highest quality. This is particularly true in the sub-millimetre where our ALMA exposures on seven targets have 0.″095 resolution combined with individual ≈0.5-h exposures. We find that:

(1) From an AGN versus SFG SED-fitting comparison and/or from the presence of an X-ray detection, 7/12 sub-mm sources are identified as quasars, 1/12 is identified as a low-redshift spiral galaxy, and 3/12 show no preference between AGN and star-forming templates, leaving 1/12 with no optical/IR/X-ray counterpart identified. Note that 2 of the 7 quasar sub-millimetre sources have previous optical spectra that identify them as quasars that also show absorbed X-ray spectra (Vallbe Mumbru 2004; Bielby et al. 2012) and that a further 3 of the 7 sources show X-ray detections at fainter levels, now positively identifying 5 out of these 7 as quasars. We conclude that most of our SMG SEDs can be as easily fitted by an obscured AGN as an obscured SFG with about half now positively identified by X-rays as obscured quasars. We re-iterate that, as shown by e.g. Dudzevičiūtė et al. (2020), good star-forming fits can likely be found for these SMGs. Our only suggestion is that AGN models are frequently found to be as good fits in simple model comparisons.

(2) 10 out of 12 sub-mm sources show MIR colours that satisfy the $[3.6]-[4.5] > 0.4$ quasar selection criteria of Stern et al. (2012), confirming the result of Dudzevičiūtė et al. (2020). However, since $z > 2$ galaxies can also occupy these MIR regions, this should again be regarded only as a consistency check rather than a proof that they are AGN.

(3) The SED fits for the sub-millimetre sources identified as AGN imply the ranges of $0.5 < z < 4.5$ for redshifts, $0 < A_V < 2.5$ mag for dust absorption, and $10 < T < 50$ K for the dust temperatures. We

note that the dust absorption implied for the two quasars with well-measured X-ray absorption is an order of magnitude higher based on their HI column, assuming Galactic gas–dust ratios than indicated by SED fitting. This suggests that the dust absorbing the optical light either does not have Galactic gas–dust ratios or is not co-located with the neutral hydrogen gas. Dust masses obtained from the SED fits are in the range of $1-5 \times 10^8 M_\odot$.

(4) We find that the MIR brightness of sub-millimetre sources is typically a factor of $\approx$10 below those of X-ray quasars although the bolometric luminosities of both populations are similar with the increased sub-millimetre emission compensating for decreased X-ray and optical emission. One explanation is that brighter quasars have less cold dust and more hot dust.

In future papers, we shall study the physical size of these sub-millimetre sources, including whether their sub-millimetre surface brightnesses are more likely to be explained by AGN or SFGs. We shall also compare these results to those for luminous quasars at high redshift ($z > 6$).

ACKNOWLEDGEMENTS

This paper makes use of the following ALMA data: ADS/JAO.ALMA/2016.1.01523.S. ALMA is a partnership of the European Southern Obseratory (representing its member states), the National Science Foundation (USA), and National Iinstitutes of Natural Sciences (Japan), together with the National Research Council (Canada), the Ministry of Science and Technology and Academia Sinica Institute of Astronomy and Astrophysics (Taiwan), and the Korea Astronomy and Space Science Institute (Republic of Korea), in cooperation with the Republic of Chile. The Joint ALMA Observatory is operated by the European Southern Observatory, Associated Universities, Inc./National Radio Astronomy Observatory and The National Astronomical Observatory of Japan. We thank an anonymous referee for very useful comments that have improved the quality of this paper.

DATA AVAILABILITY

The catalogue data underlying this article are available in the article and Appendix A. The imaging data underlying this article will be shared on reasonable request to the corresponding author.

REFERENCES

Alexander D. M., Bauer F. E., Chapman S. C., Smail I., Blain A. W., Brandt W. N., Ivison R. J., 2005, ApJ, 632, 736
Andreani P., Franceschini A., Granato G., 1999, MNRAS, 306, 161
Ansarinejad B., 2020, PhD thesis, Durham University, UK
Asboth V. et al., 2016, MNRAS, 462, 1989
Barger A. J., Cowie L. L., Sanders D. B., Fulton E., Taniguchi Y., Sato Y., Kawara K., Okuda H., 1998, Nature, 394, 248
Baugh C. M., Lacey C. G., Frenk C. S., Granato G. L., Silva L., Bressan A., Benson A. J., Cole S., 2005, MNRAS, 356, 1191
Beckwith S. V. W. et al., 2006, AJ, 132, 1729
Bielby R. M., Hill M. D., Metcalfe N., Shanks T., 2012, MNRAS, 419, 1315
Blain A. W., Smail I., Ivison R. J., Kneib J. P., Frayer D. T., 2002, Phys. Rep., 369, 111
Böhm A., Ziegler B. L., 2007, ApJ, 668, 846
Cardelli J. A., Clayton G. C., Mathis J. S., 1989, ApJ, 345, 245
Carnall A. C. et al., 2015, MNRAS, 451, L16
Chehade B. et al., 2018, MNRAS, 478, 1649
Comastri A., Setti G., Zamorani G., Hasinger G., 1995, A&A, 296, 1
Cowie L. L., González-López J., Barger A. J., Bauer F. E., Hsu L. Y., Wang W. H., 2018, ApJ, 865, 106
da Cunha E. et al., 2015, ApJ, 806, 110
Dickinson M., Giavalisco M., GOODS Team, 2003, in Bender R., Renzini A., eds, The Mass of Galaxies at Low and High Redshift. Springer-Verlag, p. 324
Dudzevičiūtė U. et al., 2020, MNRAS, 494, 3828
Dunne L., Eales S., Edmunds M., Ivison R., Alexander P., Clements D. L., 2000, MNRAS, 315, 115
Franco M. et al., 2018, A&A, 620, A152
Fritz A., Böhm A., Ziegler B. L., 2009, MNRAS, 393, 1467
Gordon K. D., Clayton G. C., Misselt K. A., Land olt A. U., Wolff M. J., 2003, ApJ, 594, 279
Grogin N. A. et al., 2011, ApJS, 197, 35
Gullberg B. et al., 2019, MNRAS, 490, 4956
Gunn K. F., Shanks T., 1999, preprint (astro–ph/9909089)
Hatziminaoglou E. et al., 2010, A&A, 518, L33
Heywood I., Bielby R. M., Hill M. D., Metcalfe N., Rawlings S., Shanks T., Smirnov O. M., 2013, MNRAS, 428, 935
Hill M. D., Shanks T., 2011a, MNRAS, 410, 762
Hill M. D., Shanks T., 2011b, MNRAS, 414, 1875
Hodge J. A. et al., 2013, ApJ, 768, 91
Hodge J. A. et al., 2016, ApJ, 833, 103
Karim A. et al., 2013, MNRAS, 432, 2
Kuraszkiewicz J. K. et al., 2003, ApJ, 590, 128
Lacey C. G., Baugh C. M., Frenk C. S., Silva L., Granato G. L., Bressan A., 2008, MNRAS, 385, 1155
Laird E. S., Nandra K., Pope A., Scott D., 2010, MNRAS, 401, 2763
Landt H., Elvis M., Ward M. J., Bentz M. C., Korista K. T., Karovska M., 2011, MNRAS, 414, 218
Le Fèvre O. et al., 2015, A&A, 576, A79
Luo B. et al., 2017, ApJS, 228, 2
Metcalfe N., Shanks T., Campos A., Fong R., Gardner J. P., 1996, Nature, 383, 236
Metcalfe N., Shanks T., Campos A., McCracken H. J., Fong R., 2001, MNRAS, 323, 795
Metcalfe N., Shanks T., Weilbacher P. M., McCracken H. J., Fong R., Thompson D., 2006, MNRAS, 370, 1257
Oliver S. J. et al., 2012, MNRAS, 424, 1614
Press W. H., Teukolsky S. A., Vetterling W. T., Flannery B. P., 1992, Numerical Recipes in FORTRAN, The Art of Scientific Computing. CUP, Cambridge
Ricci C. et al., 2017, ApJS, 233, 17
Richards G. T. et al., 2003, AJ, 126, 1131
Sawicki M., 2012, PASP, 124, 1208
Siebenmorgen R., Voshchinnikov N. V., Bagnulo S., 2014, A&A, 561, A82
Smail I., Ivison R. J., Blain A. W., 1997, ApJ, 490, L5
Stach S. M. et al., 2019, MNRAS, 487, 4648
Stern D. et al., 2012, ApJ, 753, 30
Timlin J. D. et al., 2016, ApJS, 225, 1
Vallbe Mumbru M., 2004, PhD thesis, Durham University, UK
Veilleux S. et al., 2009, ApJS, 182, 628
Wang S. X. et al., 2013, ApJ, 778, 179
Wang L. et al., 2015, MNRAS, 449, 4476
Weiß A. et al., 2009, ApJ, 707, 1201
Wright E. L. et al., 2010, AJ, 140, 1868

APPENDIX A: WHDF FLUX ERRORS, COORDINATES, AND MAGNITUDES

Here, we present further details of the WHDF data as used in the article. Table A1 supplies the WHDF flux errors appropriate for the fluxes already presented in Table 1 in the main body of the text. Tables A2 and A3 contain the RA and Declination coordinates for each ALMA counterpart or close companion (if any). Optical data from WHDF and *HST* are given along with *Chandra* X-ray and Spitzer 3.6-, 4.5-μm fluxes. Table A3 presents the equivalent data for the sources with only LABOCA data. Finally, Table A4 presents HeLMS FIR and VLA 8.4-GHz radio data for all sources detected in these bands.

Table A1. ALMA/LABOCA counterpart source flux errors in mJy corresponding to fluxes in Table 1. Rows 1–3 give the *Chandra* X-ray 0.5–1.2, 1.2–2.0, and 2.0–7.0 keV flux errors, rows 4–9 the WHDF UBRIZHK data, and rows 9,12,13, and 14 list the W1, W2, W3, and W4 band flux errors from WISE. Rows 10 and 11 give the 3.6-, 3.5-μm flux errors from SPIES and rows 15–16 list the HeLMS FIR flux errors. Row 17 gives the LABOCA sub-millimetre flux errors in mJy/beam except for LAB-12 where the ALMA flux is given. Row 17 gives the VLA 8.4-GHz flux errors.

$\lambda(\mu$m)	LAB-1	LAB-2	LAB-3	LAB-4	LAB-5	LAB-6	LAB-7	LAB-8	LAB-9	LAB-10	LAB-11	LAB-12
3.26e-4	4.89e-8	–	2.18e-8	–	6.03e-8	–	–	–	–	–	9.37e-8	–
7.95e-4	3.67e-8	–	7.60e-8	3.53e-08	1.21e-7	–	–	–	–	–	6.47e-8	–
1.14e-3	–	–	–	7.78e-08	5.20e-8	–	–	–	–	–	–	–
0.375	–	–	2.69e-5	–	6.87e-5	1.77e-2	0.116e-3	8.90e-5	–	–	1.26e-4	–
0.45	1.71e-5	1.40e-5	4.44e-5	–	4.92e-5	4.17e-2	0.154e-3	4.55e-5	–	0.45e-4	1.60e-4	–
0.65	7.84e-5	1.46e-5	1.29e-4	–	9.42e-5	1.10e-1	0.632e-4	6.48e-5	6.72e-5	8.34e-5	2.86e-4	–
0.80	1.44e-5	9.35e-5	1.39e-4	–	1.90e-4	1.93e-2	0.141e-2	–	–	–	6.38e-4	7.1e-6
0.90	–	–	–	–	–	1.94e-2	0.160e-2	–	–	–	7.52e-4	–
1.65	8.96e-4	–	7.68e-4	7.8e-4	9.0e-4	0.379	0.124e-2	–	9.72e-4	–	3.05e-3	–
2.20	–	–	–	–	3.87e-3	0.509	–	–	–	–	4.18e-3	1.5e-4
3.37	–	–	–	–	–	0.052	–	–	–	–	6.9e-3	–
3.55	3.46e-3	–	1.15e-3	1.88e-3	3.39e-3	7.50e-3	1.77e-3	–	2.4e-3	2.94e-3	3.79e-3	4.2e-3
4.49	2.15e-3	–	–	2.60e-3	2.64e-3	0.70e-2	1.55e-3	1.25e-3	2.3e-3	6.0e-4	3.39e-3	2.9e-3
4.62	–	–	–	–	–	3.28e-2	–	–	–	–	0.014	–
12.01	–	–	–	–	–	0.26	–	–	–	–	0.173	–
22.19	–	–	–	–	–	2.38	–	–	–	–	2.00	–
250	6.06	6.73	–	–	6.54	5.97	5.98	6.25	–	6.55	6.74	–
350	6.64	–	–	–	6.53	6.28	5.70	5.98	–	6.40	–	–
500	7.92	7.93	–	–	8.54	7.74	6.84	7.05	–	–	–	–
850	1.19	1.02	1.42	1.11	1.11	1.08	1.82	1.82	1.59	1.03	1.06	0.24
35461	–	4.88e-3	–	–	6.28e-3	7.55e-3	–	–	–	–	7.81e-3	4.6e-4

Table A2. LABOCA source coordinates and apparent magnitudes/colours/fluxes. For each source, row (1) shows the ALMA 870-μm coordinate and then any previous identification and redshift. Row (2) gives coordinates of any X-ray source detected in this paper and then the fluxes in the respective 0.5–1.2 keV, 1.2–2.0 keV, and 2.0–7.0 keV bands in ergs cm^{-2} s^{-1}. Brackets mean that the X-ray detection includes zero at 90% confidence. Row (3) gives the WHDF *r*-band total magnitude and aperture colours where available and as indicated at the top line of the table. WHDF *r* coordinates are shown after the addition of the $+0.''49$ and $-0.''35$ offsets required to correct them to the SDSS/ALMA/*HST*/VLA coordinate system. Row (4) provides the WHDF *H*-band coordinate if object detected at *H*. Coordinates are shown after $+0.''10$ and $-0.''38$ corrections to SDSS/ALMA/*HST*/VLA system. Row (5) indicates the detection of an *HST i*-band source, either the sub-millimetre counterpart or companion as indicated. Row (6) gives the SPIES [3.6] and [4.5] μm coordinates and fluxes in mJy when available. All magnitudes are in the Vega system.

Name	RA(J2000)	Dec	*r*	Type	*u–r*	*b–r*	*r–i*	*r–z*	*r–h*	*r–k*	3.6 μm	4.5 μm
ALMA-LAB-01(1)	00:22:37.58	00:19:18.32										
X-ray TS (2)	00:22:37.57	00:19:18.3	–	5.84e-17	7.42e-16							
whdf5449 (3)	00:22:37.57	00:19:18.35	25.44	5	–	1.71	–	–	3.79	–		
H band (4)	00:22:37.55	00:19:18.12										
$i_{\rm HST}$(5)	00:22:37.57	00:19:18.19					26.36					
3.6, 4.5 μm(6)	00:22:37.56	00:19:18.29									17.88	17.76
ALMA-LAB-02	00:22:28.44	00:21:47.61										
whdf9271	00:22:28.53	00:21:46.65	25.76	10	–	1.61	0.39	–	–	–		
$i_{\rm HST}$	00:22:28.47	00:21:46.73					25.49					
4.5 μm	00:22:28.58	00:21:47.97									–	19.53
ALMA-LAB-03	00:22:45.96	00:18:41.17										
X-ray TS	00:22:45.95	00:18:41.1	–	1.77e-16	(6.29e-17)							
whdf9547-Comp	00:22:45.94	00:18:39.65	24.15	10	1.62	1.21	0.20	–	2.33	–		
H band	00:22:45.97	00:18:40.86							≈22.8			
$i_{\rm HST}$-Comp	00:22:45.91	00:18:39.49					Double					
3.6 μm	00:22:45.86	00:18:40.95									19.95	–
ALMA LAB-04	00:22:29.19	00:20:24.79								–		
X-ray TS	00:22:29.19	00:20:24.7	1.09e-16	5.6e-17		–						
H band	00:22:29.21	00:20:25.12							21.8			
3.6, 4.5 μm	00:22:29.20	00:20:25.00									18.71	17.36

Table A2 – *continued*

Name	RA(J2000)	Dec	*r*	Type	*u–r*	*b–r*	*r–i*	*r–z*	*r–h*	*r–k*	3.6 μm	4.5 μm
ALMA-LAB-05	00:22:22.87	00:20:13.52	QSO	$z = 2.12$								
X-ray TS	00:22:22.86	00:20:13.5	1.11-16	7.18e-16	2.09e-15							
Xray/whdfch8	00:22:22.86	00:20:13.5										
whdf6483	00:22:22.83	00:20:13.05	23.57	5	−0.50	0.72	0.58	–	3.62	4.30		
H band	00:22:22.84	00:20:13.72							19.95			
3.6 μm	00:22:22.85	00:20:13.39									17.15	16.42
ALMA-LAB-10	00:22:35.23	00:24:07.52										
HST Comp	00:22:35.14	00:24:07.59					25.85					
3.6, 4.5 μm	00:22:35.10	00:24:07.24									18.48	17.48
ALMA-LAB-11	00:22:24.84	00:20:11.44	QSO	$z = 1.32$								
X-ray TS	00:22:24.84	00:20:11.4	–	2.02e-16	4.81e-15							
Xray/whdfch7	00:22:24.84	00:20:11.4										
whdf6423	00:22:24.87	00:20:11.22	22.53	6	0.37	1.00	0.99	1.36	3.72	4.54		
H band	00:22:24.84	00:20:11.62							18.81			
$i_{\rm HST}$	00:22:24.84	00:20:11.62					$''$					
3.6, 4.5 μm	00:22:24.82	00:20:11.48									16.00	15.14
ALMA-LAB-12:	00:22:25.48	00:20:06.60										
H, *K* bands	00:22:25.50	00:20:06.72							21.04	19.87		
$i_{\rm HST}$	00:22:25.46	00:20:06.95					25.38					
3.6 μm	00:22:25.57	00:20:05.85									17.69	–
4.5 μm	00:22:25.46	00:20 06.62									–	17.31

Table A3. LABOCA coordinates and apparent magnitudes/colours/fluxes for sources with no ALMA observation. For each source, row (1) shows the original LABOCA 870-μm coordinate and then any previous identification and redshift. Row (2) gives coordinates of any X-ray source detected in this paper and then the fluxes in the respective 0.5–1.2 keV, 1.2–2.0 keV, and 2.0–7.0 keV bands in ergs cm^{-2} s^{-1}. Brackets mean that the X-ray detection includes zero at 90% confidence. Row (3) gives the WHDF *R*-band magnitude and aperture colours where available and as indicated at the top line of the table. WHDF *r* coordinates that apply to both sources and images are shown after the addition of the $+0.''49$ and $-0.''35$ offsets required to correct them to the SDSS/ALMA/*HST*/VLA coordinate system. Row (4) provides the WHDF *H*-band coordinate corrected by $+0.''15$ in RA and $-0.''37$ in Dec to the SDSS/ALMA/*HST*/VLA system, if object detected at *H*. Row (5) gives the SPIES [3.6] and [4.5] μm coordinates and fluxes in mJy when available. All magnitudes are in the Vega system. For LAB-07, three possible counterparts are given with our preferred candidate being LAB-07-3.

Name	RA (J2000)	Dec	Note/ *X*/ *r*	*X*/Type	*X*/ *u–r*	*b–r*	*r–i*	*r–z*	*r–h*	*r–k*	3.6 μm	4.5 μm
WHDF-LAB-06(1)	00:22:32.09	00:21:24.3	$z = 0.046$ spiral									
X-ray TS (2)	00:22:31.85	00:21:27.6	(2.44e-17)	(6.82e-17)	(1.63e-16)							
whdf3406 (3)	00:22:31.89	00:21:27.35	16.05	7	1.61	1.45	0.59	0.91	2.36	2.63		
H band (4)	(as for whdf3406)								13.69			
3.6, 4.5 μm(5)	00:22:31.84	00:21:27.18									13.03	12.91
WHDF-LAB-07	00:22:48.49	00:16:32.8										
LAB-07-1												
X-ray TS	00:22:48.48	00:16:40.8	–	(4.75e-17)	(6.57e-16)							
whdfext6086	00:22:48.52	00:16:40.35	24.68	5	–	1.01	–	–	–	–		
3.6, 4.5 μm	00:22:48.62	00:16:40.47									18.80	18.26
LAB-07-2												
whdfext3722	00:22:48.71	00:16:34.25	24.38	5	–	0.46	–	–	2.28	–		
4.5 μm	00:22:48.67	00:16:33.98									–	19.50
LAB-07-3												
X-ray TS	00:22:48.36	00:16 28.9	(7.35e-17)	–	–							
whdfext3652	00:22:48.40	00:16:28.55	22.44	5	2.01	2.03	0.62	0.60	2.38	–		
H band	(as for whdfext3652)								20.06			
3.6, 4.5 μm	00:22:48.39	00:16:28.53									18.69	18.59
WHDF-LAB-08	00:22:29.66	00:16:05.4										
whdfext3250	00:22:29.94	00:16:06.20	25.65	5	−0.79	− 0.12	–	–	–	–		
4.5 μm	00:22:30.13	00:16:08.27									–	19.39
WHDF-LAB-09	00:22:19.90	00:17:00.1										
X-ray TS	00:22:19.90	00:17:00.1	(5.29e-17)	–	(8.98e-16)							
whdfext5230	00:22:20.02	00:16:59.60	25.61	5	–	–	–	–	4.56	–		
H band	(as for whdfext5230)								21.05			
3.6, 4.5 μm	00:22:20.00	00:16:59.57									18.84	18.25

Table A4. ALMA/LABOCA source coordinates and HeLMS + VLA positions and fluxes. Note that EVLA-6-2 is regarded as a companion to LAB-12 rather than a counterpart.

Name + Band	RA (J2000)	Dec	Flux (mJy)
ALMA-LAB-01	00:22:37.58	00:19:18.32	
250 μm	00:22:37.61	00:19:11.19	40.67
350 μm	00:22:37.61	00:19:11.65	32.07
500 μm	00:22:37.24	00:19:24.71	37.72
ALMA-LAB-02	00:22:28.44	00:21:47.61	
250 μm	00:22:27.84	00:21:30.43	20.60
500 μm	00:22:27.74	00:21:26.64	24.23
EVLA-32	00:22:28.25	00:21:47.24	1.46e-2
ALMA-LAB-05	00:22:22.87	00:20:13.52	
250 μm	00:22:22.90	00:20:15.61	32.52
350 μm	00:22:23.46	00:20:12.70	46.14
500 μm	00:22:23.49	00:20:22.87	42.34
EVLA-8	00:22:22.81	00:20:14.6	3.75e-2
WHDF-LAB-06	00:22:32.09	00:21:24.3	
250 μm	00:22:31.98	00:21:26.58	129.8
350 μm	00:22:31.86	00:21:26.50	39.59
500 μm	00:22:32.94	00:21:25.35	25.57
EVLA:01	00:22:31.86	00:21:27.5	2.01e-1
WHDF-LAB-07	00:22:48.49	00:16:32.8	
250 μm	00:22:47.84	00:16:31.83	91.10
350 μm	00:22:47.94	00:16:29.67	72.04
500 μm	00:22:47.72	00:16:34.98	61.61
WHDF-LAB-08	00:22:29.66	00:16:05.4	
250 μm	00:22:30.07	00:16:10.89	42.49
350 μm	00:22:30.07	00:16:08.98	54.0
500μm	00:22:30.23	00:16:09.57	39.64
ALMA-LAB-10	00:22:35.23	00:24:07.52	
250 μm	00:22:35.59	00:24:09.60	22.18
350 μm	00:22:35.36	00:24:11.00	27.74
ALMA-LAB-11	00:22:24.84	00:20:11.44	
250 μm	00:22:25.29	00:20:08.92	44.00
EVLA-6	00:22:24.89	00:20:10.21	4.6e-2
ALMA-LAB-12:	00:22:25.48	00:20:06.60	
EVLA-6-2	00:22:25.75	00:20:01.69	7.6e-3

Table A4 – *continued*

This paper has been typeset from a TEX/LATEX file prepared by the author.